
p -Multigrid matrix-free discontinuous Galerkin solution strategies for the under-resolved simulation of incompressible turbulent flows

M. Franciolini^{a,*}, L. Botti^b, A. Colombo^b, A. Crivellini^a

^a *Dipartimento di Ingegneria Industriale e Scienze Matematiche,
Università Politecnica delle Marche, Ancona 60131, Italy*

^b *Dipartimento di Ingegneria e Scienze Applicate,
Università degli Studi di Bergamo, 24044 Dalmine (BG), Italy*

Abstract

In recent years several research efforts focused on the development of high-order discontinuous Galerkin (dG) methods for scale resolving simulations of turbulent flows. Nevertheless, in the context of incompressible flow computations, the computational expense of solving large scale equation systems characterized by indefinite Jacobian matrices has often prevented from dealing with industrially-relevant computations. In this work we seek to improve the efficiency of Rosenbrock-type linearly-implicit Runge-Kutta methods by devising robust, scalable and memory-lean solution strategies. In particular, we combined p -multigrid preconditioners with matrix-free Krylov iterative solvers: the p -multigrid preconditioner relies on specifically crafted rescaled-inherited coarse operators and cheap block-diagonal smoother's preconditioners to obtain satisfactory convergence rates and a low memory occupation. Extensive numerical validation is performed. The rescaled-inherited p -multigrid algorithm for the BR2 dG discretization is firstly validated solving Poisson problems. The Rosenbrock formulation is then applied to test cases of growing complexity: the laminar unsteady flow around a two-dimensional cylinder at $Re = 200$ and around a sphere at $Re = 300$, and finally the transitional T3L1 flow problem of the ERCOFTAC test case suite with different levels of free-stream turbulence. For the latter good agreement with experimental data is documented, moreover, strong memory savings and execution time gains with respect to state-of-the art preconditioners are reported.

Keywords: incompressible flows, implicit LES, discontinuous Galerkin, p -multigrid, matrix-free, parallel efficiency

*Corresponding author: m.franciolini@pm.univpm.it
Preprint submitted to Journal

1. Introduction

In recent years the increasing availability of High Performance Computing (HPC) resources strongly promoted the widespread of Large Eddy Simulation (LES) turbulence modelling approaches. In particular, Implicit LES (ILES) based on discontinuous Galerkin (dG) spatial discretizations showed very promising results due to the favourable dispersion and dissipation properties of the method [1]. The high potential of dG approximations for the under-resolved simulation of turbulent flows has been demonstrated in the literature for those moderate Reynolds numbers conditions where Reynolds-averaged Navier–Stokes (RANS) approaches are known to fall short, *e.g.*, massively separated flows [2, 3].

Research on this topic is growing fast and several efforts focused on devising efficient time integration strategies suited for massively parallel architectures. Indeed, the inherently unsteady nature of LES/ILES and the need to reduce time-to-results pose serious challenges to the achievement of cost effective scale-resolving computations and the ability to fruitfully exploit large computational facilities. In this context high-order implicit time integration schemes are attractive to overcome the strict stability limits of explicit methods when dealing with high-degree polynomial approximations, [4, 5, 6]. Nevertheless, implicit schemes require to solve large non-linear/linear systems of equations. The sparsity pattern of the global system matrix imposes the use of iterative methods, indeed the number of non-zeros scales as k^6 , where k is the degree of dG polynomial spaces. As a result high-order accurate computations for industrially relevant application turns out to be highly memory intensive and expensive from the CPU time point of view, even when employing state-of-the-art iterative solvers and modern HPC facilities.

Previous studies considered the possibility of using memory-saving implementations of the iterative solver. In [7], a matrix-free GMRES solver was used to solve steady compressible flows. In matrix-free algorithms the coefficient matrix of a linear system is not stored explicitly, but accesses by evaluating matrix-vector products. The strategy showed significant memory savings, while being at the same time competitive on the overall computational efficiency for sufficiently high-order polynomial approximations when using ILU(0) and Additive Schwarz preconditioners. In [8] a matrix-free approach is employed in the context of several time integration strategies with applications to unsteady, laminar two-dimensional problems. In [9] the use of a matrix-free GMRES is proposed for the solution of both the primal and adjoint problem with applications to compressible Navier–Stokes equations.

Recently the use of a matrix-free implementation was explored and compared to a matrix-based approach in the context of incompressible unsteady turbulent flows, see [10, 11]. In particular the solution of the Rayleigh–Benard convection problem and turbulent channel flows at moderately high Reynolds numbers was considered coupling matrix-free with cheap element-wise Block-Jacobi (EWBJ) preconditioners. Unfortunately, when dealing with stiff problems, *e.g.*, stretched elements, low Mach flows or large time step, a severe convergence degradation is observed when using EWBJ preconditioners: the solution is achieved only after a considerable number of iterations.

Multilevel methods have been considered in the past as an efficient way to solve both linear and non-linear problems arising from high-order discontinuous Galerkin discretizations. Such methods were first proposed in a dG context by Helenbrook *et al.* [12], Bassi and Rebay [13], Fidkowski *et al.* [14]. Those authors focused on the analysis of a p -multigrid (p -MG) non-linear solver, proving convergence properties and performance in the context of compressible flows using element- or line-Jacobi smoothing. Several authors also considered multigrid operators built on agglomerated coarse grids, such as h -multigrid, see for example [15, 16, 17]. The possibil-

ity of using multigrid operators as a preconditioner was also explored in the context of steady compressible flows, see for example [18, 19]. In these works, the algorithm is reported as the most efficient and scalable if compared to single-grid preconditioners, and a large reduction in the number of iteration to reach convergence was achieved. More recently, an h -multigrid preconditioner was proposed in [20] in the context of steady and unsteady incompressible flows. In this latter work a specific treatment for inherited dG discretizations of viscous terms on coarse levels was introduced, significantly improving the performance of the multigrid iteration.

The aim of the present paper is to extend the memory-saving implementation proposed in [10, 7] to deal with stiff unsteady turbulent flow problems. The time-accurate numerical framework relies on linearly-implicit Runge–Kutta schemes of the Rosenbrock type. This class of schemes requires the solution of a linear systems at each stage while the matrix is assembled only once per time step. For the linear systems solution we rely on a matrix-free implementation of the Flexible GMRES (FGMRES) method, coupled with a p -MG preconditioner. In particular, the p -multigrid iteration is built using a matrix-free GMRES smoother on the finest level, and standard matrix-based GMRES smothers on coarser levels. The h -rescaled-inherited approach proposed in [20] is here extended to the p version of the multigrid preconditioner and its impact on the convergence of the iterative method investigated. Target applications involve the high-order accurate ILES of complex flow configurations using unstructured meshes made of severely stretched and curved elements. In this paper we demonstrate the effectiveness of the proposed coupling between a matrix-free linear solver and a p -multigrid preconditioner showing large benefits both in terms of the iterative solver convergence rate and of the CPU time while maintaining a favourable memory footprint.

The paper is structured as follows. Section 2 describes the space and time discretization and presents the multigrid framework here employed, with particular attention to the coarse spaces assembly, the rescaled-inherited approach and the intergrid transfer operators. Sections 3.1 and 3.2 report a thorough assessment of the stabilization scaling on test cases of growing complexity, both steady and unsteady: the Poisson problem, the unsteady flow over a two dimensional cylinder at $Re = 200$, and the unsteady flow over a sphere at $Re = 300$. Finally, Section 3.3 demonstrates the advantages of using the proposed solver for the solution of the T3L1 flow problem of the ERCOFTAC test case suites, *i.e.*, the incompressible turbulent flow over a rounded leading-edge flat plate at $Re = 3450$ with different levels of free-stream turbulence. After a brief physical discussion of the solution accuracy, we report significant memory savings as well as improvements in computational efficiency with respect to matrix-based methods.

2. The numerical framework

In this section the space and time discretizations of the incompressible Navier–Stokes (INS) equations are briefly introduced together with a detailed description of the main building blocks of the p -multigrid preconditioner.

2.1. The dG discretization

We consider the unsteady INS equations in conservation form with Dirichlet and Neumann boundary conditions in a fixed Cartesian reference frame,

$$\partial_t \mathbf{u} + \nabla \cdot (\mathbf{u} \otimes \mathbf{u} + p \mathbf{I}) - \nu \nabla \cdot \left[(\nabla \otimes \mathbf{u} + (\nabla \otimes \mathbf{u})^t) - \frac{2}{3} (\nabla \cdot \mathbf{u}) \mathbf{I} \right] = 0 \quad \text{in } \Omega \times (0, t_F), \quad (1a)$$

$$\nabla \cdot \mathbf{u} = 0 \quad \text{in } \Omega \times (0, t_F), \quad (1b)$$

$$\mathbf{u} = \mathbf{f} \quad \text{on } \partial\Omega_D \times (0, t_F), \quad (1c)$$

$$\left[\nu (\nabla \otimes \mathbf{u} + (\nabla \otimes \mathbf{u})^t) - \frac{2}{3} \nu (\nabla \cdot \mathbf{u}) \mathbf{I} \right] \cdot \mathbf{n} = 0, \quad p \mathbf{n} = \mathbf{g} \quad \text{on } \partial\Omega_N \times (0, t_F), \quad (1d)$$

$$\mathbf{u}(\cdot, t = 0) = \mathbf{u}^0 \quad \text{in } \Omega. \quad (1e)$$

where $\mathbf{u} \in \mathbb{R}^d$ is the velocity vector, p is the pressure, $\nu > 0$ denotes the (constant) viscosity, \mathbf{u}^0 is the initial condition, t_F is the final simulation time, \mathbf{n} is the unit outward normal to $\partial\Omega$ and $\mathbf{I} = \delta_{ij} \mathbf{e}_i \otimes \mathbf{e}_j$, $i, j = 1, \dots, d$, is the identity matrix. The density has been assumed to be uniform and equal to one and the Stokes hypothesis is used for the definition of viscous stresses.

Regarding boundary conditions in (1c)-(1d), \mathbf{f} and \mathbf{g} are the boundary data to be imposed on Dirichlet and Neumann boundaries, respectively, such that $\partial\Omega_D \cup \partial\Omega_N = \partial\Omega$. In the case that $\partial\Omega_D = \partial\Omega$, we also require $\langle p \rangle_\Omega = 0$, where $\langle \cdot \rangle_\Omega$ denotes the mean value over Ω . Note that, while using the divergence free constraint (1b) we get

$$\nu \nabla \cdot \left[(\nabla \otimes \mathbf{u} + (\nabla \otimes \mathbf{u})^t) - \frac{2}{3} (\nabla \cdot \mathbf{u}) \mathbf{I} \right] = \nu \nabla^2 \mathbf{u},$$

this simplification is unsuitable for Neumann boundaries.

Introducing the convective and viscous flux functions

$$\begin{aligned} \mathbf{F}^v \left(\frac{\partial u_i}{\partial x_j} \right) &= \nu (\nabla \otimes \mathbf{u} + (\nabla \otimes \mathbf{u})^t) - \frac{2}{3} \nu (\nabla \cdot \mathbf{u}) \mathbf{I} = \nu \left(\frac{\partial u_j}{\partial x_i} + \frac{\partial u_i}{\partial x_j} - \frac{2}{3} \frac{\partial u_k}{\partial x_k} \delta_{ij} \right) \mathbf{e}_i \otimes \mathbf{e}_j \\ \mathbf{F}^c(u_i, p) &= \mathbf{u} \otimes \mathbf{u} + p \mathbf{I} = (u_i u_j + p \delta_{ij}) \mathbf{e}_i \otimes \mathbf{e}_j \end{aligned} \quad (2)$$

Eqs. (1a)-(1b) can be compactly rewritten in integral form as

$$\begin{aligned} \int_{\Omega} \partial_t \mathbf{u} + \int_{\Omega} \nabla \cdot (\mathbf{F}^c - \mathbf{F}^v) &= \mathbf{0}, \\ \int_{\Omega} \nabla \cdot \mathbf{u} &= 0. \end{aligned}$$

In order to define the dG discretization we introduce a triangulation \mathcal{T}_h of the computational domain Ω , that is the collection of disjoint mesh elements $\kappa \in \mathcal{T}_h$ such that $\bigcup_{\kappa \in \mathcal{T}_h} \bar{\kappa} = \Omega_h$, where Ω_h is a suitable approximation of Ω . The mesh skeleton \mathcal{F}_h is the collection of mesh faces σ . Internal faces $\sigma \in \mathcal{F}_h^i$ are defined as the intersection of the boundary of two neighboring elements: $\sigma = \partial\kappa \cap \partial\kappa'$ with $\kappa \neq \kappa'$. Boundary faces $\sigma \in \mathcal{F}_h^b$ reads $\sigma = \partial\kappa \cap \partial\Omega_h$. Clearly $\mathcal{F}_h = \mathcal{F}_h^i \cup \mathcal{F}_h^b$.

Each component of the velocity vector and the pressure is sought (for $0 < t < t_F$) in the so called *broken polynomial spaces* defined over \mathcal{T}_h

$$\mathbb{P}_d^k(\mathcal{T}_h) = \left\{ v_h \in L^2(\Omega_h) \mid \forall \kappa \in \mathcal{T}_h, v_h|_{\kappa} \in \mathbb{P}_d^k(\kappa) \right\} \quad (4)$$

where $\mathbb{P}_d^k(\kappa)$ is the space of polynomial functions in d variables and total degree k defined over κ . Since no continuity requirements are enforced at inter-element boundaries, v_h admits two-valued traces on the partition of mesh skeleton \mathcal{F}_h^i . Accordingly we introduce average and jump operators over internal faces

$$\text{Average} : \llbracket v_h \rrbracket_\sigma = \frac{1}{2} (v_h|_\kappa + v_h|_{\kappa'}), \quad \text{Jump} : \llbracket v_h \rrbracket_\sigma = (v_h|_\kappa - v_h|_{\kappa'}). \quad (5)$$

Specific definitions of averages and jumps will be introduced over boundary faces to take into account Dirichlet and Neumann boundary conditions.

The dG discretization of the Navier-Stokes equations reads: find $(\mathbf{u}_h, p_h) \in [\mathbb{P}^k(\mathcal{T}_h)]^d \times \mathbb{P}^k(\mathcal{T}_h)$ such that, for all $(\mathbf{v}_h, q_h) \in [\mathbb{P}^k(\mathcal{T}_h)]^d \times \mathbb{P}^k(\mathcal{T}_h)$:

$$\begin{aligned} \sum_{\kappa \in \mathcal{T}_h} \int_\kappa \partial_t \mathbf{u}_h \cdot \mathbf{v}_h - \sum_{\kappa \in \mathcal{T}_h} \int_\kappa (\mathbf{F}_h^c - \widetilde{\mathbf{F}}_h^v) : \nabla_h \mathbf{v}_h + \sum_{\sigma \in \mathcal{F}_h} \int_\sigma \mathbf{n}^\sigma \cdot (\widehat{\mathbf{F}}_h^c - \widehat{\mathbf{F}}_h^v) \cdot \llbracket \mathbf{v}_h \rrbracket &= 0, \\ - \sum_{\kappa \in \mathcal{T}_h} \int_\kappa \mathbf{u}_h \cdot \nabla_h q_h + \sum_{\sigma \in \mathcal{F}_h} \int_\sigma \mathbf{n}^\sigma \cdot \widehat{\mathbf{u}}_h \llbracket q_h \rrbracket &= 0, \end{aligned} \quad (6)$$

where $\llbracket v_h \rrbracket = \llbracket v_{h,i} \rrbracket \mathbf{e}_i$ and \mathbf{n}^σ is the normal vector with respect to σ . While obtaining (6) from (3) follows the standard dG FE practice (element-by-element integration by parts after having multiplied by a suitable test function), the dG method hinges on the definition of suitable numerical viscous $\widetilde{\mathbf{F}}_h^v$, $\widehat{\mathbf{F}}_h^v$ and inviscid fluxes $\widehat{\mathbf{F}}_h^c$, $\widehat{\mathbf{u}}_h$.

According to the BR1 scheme, proposed in [21], $\forall \boldsymbol{\tau}_h \in [\mathbb{P}_d^k(\mathcal{T}_h)]^d$, $v_h \in \mathbb{P}_d^k(\mathcal{T}_h)$, the consistent gradient $\mathbf{G}_h(v_h)$ is such that

$$\int_\Omega (\mathbf{G}_h(v_h) - \nabla v_h) \cdot \boldsymbol{\tau}_h = - \sum_{\sigma \in \mathcal{F}_h} \int_\sigma \llbracket v_h \rrbracket \llbracket \boldsymbol{\tau}_h \rrbracket \cdot \mathbf{n}^\sigma = \sum_{\sigma \in \mathcal{F}_h} \int_\Omega \mathbf{r}^\sigma(\llbracket v_h \rrbracket) \cdot \boldsymbol{\tau}_h = \sum_{\kappa \in \mathcal{T}_h} \int_\kappa \mathbf{R}^\kappa(v_h) \cdot \boldsymbol{\tau}_h$$

where $\mathbf{r}^\sigma(\llbracket v_h \rrbracket) : \mathbb{P}_d^k(\sigma) \rightarrow [\mathbb{P}_d^k(\mathcal{T}_h)]^d$ is the local lifting operator, $\mathbf{R}^\kappa(v_h) := \sum_{\sigma \in \mathcal{F}_{\partial\kappa}} \mathbf{r}^\sigma(\llbracket v_h \rrbracket)$ is

the elemental lifting operator and $\mathcal{F}_{\partial\kappa}$ is the set of faces belonging to $\partial\kappa$. In this work we rely on the BR2 scheme, introduced to reduce the stencil of the BR1 discretization and analyzed in the context of the Poisson problem by [22] and [23]. The BR2 viscous fluxes are functions of elemental spatial derivatives corrected by suitable lifting operator contributions

$$\widetilde{\mathbf{F}}_h^v = \mathbf{F}^v \left(\frac{\partial u_{h,i}}{\partial x_j} - \mathbf{R}_j^\kappa(u_{h,i}) \right), \quad \text{and} \quad \widehat{\mathbf{F}}_h^v = \mathbf{F}^v \left(\left\{ \left\{ \frac{\partial u_{h,i}}{\partial x_j} - \eta_\sigma r_j^\sigma(\llbracket u_{h,i} \rrbracket) \right\} \right\} \right), \quad (7)$$

$\widehat{\mathbf{F}}_h^v$ ensures consistency and stability of the scheme and $\widetilde{\mathbf{F}}_h^v$ guarantees the symmetry of the formulation. As proved by Brezzi *et al.* [22], coercivity for the BR2 discretization of the Laplace equation holds provided that η_σ is greater than the maximum number of faces of the elements sharing σ . In order to impose boundary conditions on $\sigma \in \mathcal{F}_h^b$, viscous fluxes reads

$$\text{Dirichlet} : \quad \widehat{\mathbf{F}}_h^v = \mathbf{F} \left(\frac{\partial u_{h,i}}{\partial x_j} - \eta_\sigma r_j^\sigma(\llbracket u_{h,i} \rrbracket) \right), \quad \llbracket \mathbf{u}_h \rrbracket_\sigma = (\mathbf{u}_h|_\kappa - \mathbf{f}). \quad (8)$$

$$\text{Neumann} : \quad \mathbf{n}^\sigma \cdot \mathbf{F}_h^v = 0, \quad \llbracket \mathbf{u}_h \rrbracket_\mathbf{f} = 0.$$

The inviscid numerical fluxes of the dG discretization result from the exact solution of local Riemann problems based on an artificial compressibility perturbation of the Euler equations,

as proposed in [24]. Boundary conditions for inviscid fluxes are enforced weakly by properly defining a ghost boundary state $(\mathbf{u}_{gb}, p_{gb})$ having support on the interface $\sigma \in \mathcal{F}_h^b$ of a ghost neighboring elements κ_g . The ghost boundary state is defined imposing the conservation of Riemann invariants based on the hyperbolic nature of the artificial compressibility perturbation of the Euler equation. Accordingly, both the internal state $(\mathbf{u}^\kappa, p^\kappa)$ and the boundary data $(\mathbf{f}$ or \mathbf{g} , in case of Dirichlet or Neumann boundary conditions, respectively) are involved in the definition of $(\mathbf{u}_{gb}, p_{gb})$. We remark that, since the performance of the inherited p -multigrid strategy here considered is mostly affected by projections of viscous flux operators, it is not relevant to provide additional details regarding the inviscid flux treatment.

2.2. Implicit time accurate integration

The accurate time integration of the spatially dG discretized INS equations can be presented in compact form by collecting the velocity vector and the pressure polynomial expansions in the vector $\mathbf{w}_h \stackrel{\text{def}}{=} (u_{h,1}, \dots, u_{h,d}, p_h) \in [\mathbb{P}_d^k(\mathcal{T}_h)]^{d+1}$ and identifying the unknown vector at time t_n with \mathbf{w}_h^n , that is $\mathbf{w}_h^n = [\mathbf{u}_h(t_n), p_h(t_n)]$. Moreover, we introduce the flux functions $\widetilde{\mathbf{F}}_h(\mathbf{w}_h) \stackrel{\text{def}}{=} [\mathbf{F}_h^c - \widetilde{\mathbf{F}}_h^v, \mathbf{u}_h] \in \mathbb{R}^d \otimes \mathbb{R}^{d+1}$ and $\widehat{\mathbf{F}}_h(\mathbf{w}_h) \stackrel{\text{def}}{=} [\widehat{\mathbf{F}}_h^c - \widehat{\mathbf{F}}_h^v, \widehat{\mathbf{u}}_h] \in \mathbb{R}^d \otimes \mathbb{R}^{d+1}$, collecting the viscous and inviscid flux contributions. For all $\mathbf{w}_h, \mathbf{z}_h \in [\mathbb{P}_d^k(\mathcal{T}_h)]^{d+1}$, we define the residual of the dG spatial discretization in (6) as follows

$$f_h(\mathbf{w}_h, \mathbf{z}_h) = - \sum_{\kappa \in \mathcal{T}_h} \int_{\kappa} \sum_{i=1}^{d+1} \sum_{p=1}^d \widetilde{F}_{p,i}(\mathbf{w}) \frac{\partial z_i}{\partial x_p} + \sum_{\sigma \in \mathcal{F}_h} \int_{\sigma} \sum_{i=1}^{d+1} \sum_{p=1}^d n_p^\sigma \widehat{F}_{p,i}(\mathbf{w}) \llbracket z_i \rrbracket, \quad (9)$$

where we dropped the mesh step size subscript when working in index notation. For all $\mathbf{w}_h, \delta \mathbf{w}_h, \mathbf{z}_h \in [\mathbb{P}_d^k(\mathcal{T}_h)]^{d+1}$, the Jacobian of the residual reads $j_h(\mathbf{w}_h, \delta \mathbf{w}_h, \mathbf{z}_h) = \frac{\partial f_h(\mathbf{w}_h, \mathbf{z}_h)}{\partial \mathbf{w}_h} \delta \mathbf{w}_h$. In particular we distinguish the inviscid $j_h^{iv}(\mathbf{w}_h, \delta \mathbf{w}_h, \mathbf{z}_h)$ and the viscous $j_h^{iv}(\delta \mathbf{w}_h, \mathbf{z}_h)$ contributions

$$j_h^{iv}(\mathbf{w}_h, \delta \mathbf{w}_h, \mathbf{z}_h) = - \sum_{\kappa \in \mathcal{T}_h} \int_{\kappa} \sum_{i,j=1}^{d+1} \sum_{p=1}^d \frac{\partial \widetilde{F}_{p,i}}{\partial w_j}(\mathbf{w}_h) \delta w_j \frac{\partial z_i}{\partial x_p} + \sum_{\sigma \in \mathcal{F}_h} \int_{\sigma} \sum_{i,j=1}^{d+1} \sum_{p=1}^d n_p^\sigma \frac{\partial \widehat{F}_{p,i}}{\partial w_j}(\mathbf{w}_h) \delta w_j \llbracket z_i \rrbracket, \quad (10)$$

$$\begin{aligned} j_h^{iv}(\delta \mathbf{w}_h, \mathbf{z}_h) = & - \sum_{\kappa \in \mathcal{T}_h} \int_{\kappa} \sum_{i,j=1}^{d+1} \sum_{p,q=1}^d \frac{\partial \widetilde{F}_{p,i}}{\partial (\partial w_j / \partial x_q - R_q^\kappa(w_j))} \left(\frac{\partial (\delta w_j)}{\partial x_q} - R_q^\kappa(\delta w_j) \right) \frac{\partial z_i}{\partial x_p} + \\ & + \sum_{\sigma \in \mathcal{F}_h} \int_{\sigma} \sum_{i,j=1}^{d+1} \sum_{p,q=1}^d n_p^\sigma \frac{\partial \widehat{F}_{p,i}}{\partial (\partial w_j / \partial x_q - \eta_{\sigma} r_q^\sigma(w_j))} \left\{ \left\{ \frac{\partial (\delta w_j)}{\partial x_q} - \eta_{\sigma} r_q^\sigma(\llbracket \delta w_j \rrbracket) \right\} \right\} \llbracket z_i \rrbracket. \end{aligned} \quad (11)$$

Note that, since \mathbf{F}^v is a linear function, (11) is a bilinear form, while, by abuse of notation, (10) is a bilinear (resp. trilinear) when $F_{p,i}^c(\mathbf{w})$ is a linear (resp. non-linear) function of w_j .

In this work time accurate integration is performed via the multi-stage linearly implicit (Rosenbrock-type) Runge-Kutta method. As an appealing feature the method requires the solution of a linear system at each stage $s = \{1, \dots, n_s\}$, while the Jacobian matrix needs to be assembled only once per time step. Prior to introducing the formulation for the temporal discretization we define the following mass bilinear form: for all $\mathbf{w}_h, \mathbf{z}_h \in [\mathbb{P}_d^k(\mathcal{T}_h)]^{d+1}$

$$m_h(\mathbf{w}_h, \mathbf{z}_h) = \sum_{\kappa \in \mathcal{T}_h} \int_{\kappa} \sum_{i=1}^d w_i z_i. \quad (12)$$

Given the initial condition $\mathbf{w}_h^0 = \mathbf{w}_h(t = 0) \in [\mathbb{P}^k(\mathcal{T}_h)]^{d+1}$ we define the sequence \mathbf{w}_h^{n+1} iteratively by means of the Rosenbrock scheme as described in the following algorithm.

Algorithm 1 Multi-stage linearly implicit (Rosenbrock-type) Runge-Kutta method

```

1: set  $\mathbf{w}_h^n = \mathbf{w}_h^0$ ,  $n_F = \frac{t_F}{\delta t}$ 
2: for  $n = 0, \dots, n_F$  do
3:   for  $s = 1, \dots, n_s$  do
4:     set  $\delta \mathbf{p}_h = \mathbf{0} \wedge \delta \mathbf{q}_h = \mathbf{0}$ 
5:     for  $o = 1, \dots, s - 1$  do
6:        $\delta \mathbf{p}_h += \mathbf{a}_{s,o} \delta \mathbf{w}_h^o$ 
7:        $\delta \mathbf{q}_h += \mathbf{c}_{s,o} \delta \mathbf{w}_h^o$ 
8:     end for
9:     find  $\delta \mathbf{w}_h^s \in [\mathbb{P}^k(\mathcal{T}_h)]^{d+1}$  such that, for all  $\mathbf{z}_h \in [\mathbb{P}^k(\mathcal{T}_h)]^{d+1}$ 
       
$$\frac{1}{\gamma \delta t} m_h(\delta \mathbf{w}_h^s, \mathbf{z}_h) + j_h(\mathbf{w}_h^n, \delta \mathbf{w}_h^s, \mathbf{z}_h) = -f_h(\mathbf{w}_h^n + \delta \mathbf{p}_h, \mathbf{z}_h) - \frac{1}{\delta t} m_h(\delta \mathbf{q}_h, \mathbf{z}_h) \quad (13)$$

10:    end for
11:    for  $o = 1, \dots, s$  do
12:      set  $\mathbf{w}_h^{n+1} = \mathbf{w}_h^n + \mathbf{m}_o \delta \mathbf{w}_h^o$ 
13:    end for
14:  end for

```

where γ , \mathbf{a}_{ij} , \mathbf{c}_{ij} and \mathbf{m}_i are real coefficients proper of the Rosenbrock scheme and $\delta \mathbf{w}_h^s$, with $s = \{1, \dots, n_s\}$, the solutions at each stage of the scheme that are properly combined to compute the solution \mathbf{w}_h^{n+1} at the next time level. The Rosenbrock time marching strategy in Algorithm 1 advances the solution in time by repeatedly solving the linearized system of equations(13), once for each stage of the Runge-Kutta method. Introducing the Jacobian and mass matrix operators

$$\begin{aligned} (\mathbf{J}_h \delta \mathbf{w}_h, \mathbf{z}_h)_{L^2(\Omega)} &= j_h(\mathbf{w}_h, \delta \mathbf{w}_h, \mathbf{z}_h) \quad \forall \mathbf{w}_h, \delta \mathbf{w}_h, \mathbf{z}_h \in [\mathbb{P}_d^{k_\ell}(\mathcal{T}_h)]^{d+1}, \\ (\mathbf{M}_h \delta \mathbf{w}_h, \mathbf{z}_h)_{L^2(\Omega)} &= m_h(\delta \mathbf{w}_h, \mathbf{z}_h) \quad \forall \delta \mathbf{w}_h, \mathbf{z}_h \in [\mathbb{P}_d^{k_\ell}(\mathcal{T}_h)]^{d+1}, \end{aligned} \quad (14)$$

the equation system (13) can be compactly rewritten as follows:

$$\mathbf{G}_h \delta \mathbf{w}_h = \mathbf{g}_h \quad (15)$$

where $\mathbf{G}_h = \frac{1}{\gamma \delta t} \mathbf{M}_h + \mathbf{J}_h$ is the global matrix operator, and $\delta \mathbf{w}_h, \mathbf{g}_h \in [\mathbb{P}_d^k(\mathcal{T}_h)]^{d+1}$ are the unknown polynomial function and the right-hand side arising from the linearly-implicit Runge-Kutta time discretization, respectively. In this work the four stages, order three (ROSI2PW) scheme of Rang and Angermann [25] was employed. This scheme preserves its formal accuracy when applied to the system of DAEs arising from the spatial discretization of the INS equations.

2.3. Multigrid preconditioners

In this work we investigate the possibility to solve the global equation system (15) by means of a FGMRES iterative solver preconditioned with p -multigrid. Since the linearized equations system needs to be repeatedly solved at each time step, the efficiency of the linear solver strategy is of crucial importance for the effectiveness of the whole method. The basic idea is to exploit iterative solvers to smooth-out the high-frequency component of the error with respect to the

unknown exact solution. Indeed, being iterative solvers not effective at damping low-frequency error components, the iterative solution of coarser problems is exploited to circumvent this issue, thus shifting the low-frequency modes towards the upper side of the spectrum. This simple and effective strategy allows to obtain satisfactory rates of convergence all along the iterative process.

In p -multigrid the coarse problems are built based on lower-order dG discretizations with respect to the original problem of degree k . We consider L coarse levels spanned by the index $\ell = 1, \dots, L$ and indicate the fine and coarse levels with $\ell = 0$ and $\ell = L$, respectively. The polynomial degree of level ℓ is k_ℓ and the polynomial degrees of the coarse levels are chosen such that $k_\ell < k_{\ell-1}$, $l = 1, \dots, L$, with $k_0 = k$. Accordingly the polynomial spaces associated to the coarse levels read $\mathbb{P}_d^{k_\ell}(\mathcal{T}_h)$. The coarse problems corresponding to (15) are in the form

$$\mathbf{G}_\ell \delta \mathbf{w}_\ell = \mathbf{g}_\ell \quad (16)$$

where \mathbf{G}_ℓ is the global matrix operator on level l and $\delta \mathbf{w}_\ell, \mathbf{g}_\ell \in [\mathbb{P}_d^{k_\ell}(\mathcal{T}_h)]^{d+1}$ are the unknown function and the known right-hand side, respectively.

A crucial aspect for the efficiency of the p -multigrid iteration is related to the computational cost of building coarse grid operators \mathbf{G}_ℓ . While it is possible to assemble the bilinear and trilinear forms j_h, f_h and m_h of Section 2.2 on each level ℓ with the corresponding polynomial functions $\mathbf{w}_h, \delta \mathbf{w}_h, \mathbf{z}_h \in \mathbb{P}_d^{k_\ell}(\mathcal{T}_h)$, significantly better performances are achievable by *restricting* the fine grid operator by means of so called Galerkin projections. The former and the latter strategies are named non-inherited and inherited p -multigrid, respectively. As will be clear in what follows the construction of coarse operators is trivial when polynomial expansions are based on hierarchical orthonormal modal basis functions.

2.3.1. Restriction and prolongation operators

In this section we describe the prolongation and restriction operators required to map polynomial functions on finer and coarser levels, respectively.

Since $\mathbb{P}_d^{k_\ell}(\mathcal{T}_h) \supset \mathbb{P}_d^{k_{\ell+1}}(\mathcal{T}_h)$, the *prolongation* operator $\mathcal{I}_{\ell+1}^\ell : \mathbb{P}_d^{k_{\ell+1}}(\mathcal{T}_h) \rightarrow \mathbb{P}_d^{k_\ell}(\mathcal{T}_h)$, is the injection operator such that

$$\sum_{\kappa \in \mathcal{T}_h} \int_{\kappa} (\mathcal{I}_{\ell+1}^\ell w_h - w_h) = 0, \quad \forall w_h \in \mathbb{P}_d^{k_{\ell+1}}(\mathcal{T}_h),$$

The prolongation operator from level ℓ to level 0 can be recursively defined by the composition of inter-grid prolongation operators: $\mathcal{I}_\ell^0 = \mathcal{I}_1^0 \mathcal{I}_2^1 \dots \mathcal{I}_\ell^{\ell-1}$.

The (L^2 projection) *restriction* operator $\mathcal{I}_\ell^{\ell+1} : \mathbb{P}_d^{k_\ell}(\mathcal{T}_h) \rightarrow \mathbb{P}_d^{k_{\ell+1}}(\mathcal{T}_h)$, is such that

$$\sum_{\kappa \in \mathcal{T}_h} \int_{\kappa} (\mathcal{I}_\ell^{\ell+1} w_h - w_h) z_h = 0, \quad \forall w_h \in \mathbb{P}_d^{k_\ell}(\mathcal{T}_h), \quad \forall z_h \in \mathbb{P}_d^{k_{\ell+1}}(\mathcal{T}_h), \quad (17)$$

and the restriction operator from level 0 to level ℓ reads $\mathcal{I}_0^\ell = \mathcal{I}_{\ell-1}^\ell \dots \mathcal{I}_1^2 \mathcal{I}_0^1$.

When applied to vector functions $\mathbf{w}_h \in [\mathbb{P}_d^{k_{\ell+1}}(\mathcal{T}_h)]^{d+1}$ the interpolation operators act componentwise, e.g., $\mathcal{I}_{\ell+1}^\ell \mathbf{w}_h = \sum_{i=1}^{d+1} \mathcal{I}_{\ell+1}^\ell w_i$. It is interesting to remark that using hierarchical orthonormal modal basis functions restriction and prolongation operators are trivial, in particular restriction from $\mathbb{P}_d^{k_\ell}(\mathcal{T}_h)$ into $\mathbb{P}_d^{k_{\ell+1}}(\mathcal{T}_h)$ is as simple as keeping the degrees of freedom of the modes of order $k \leq k_{\ell+1}$ and discarding the remaining high-frequency modes.

2.4. Fine and coarse grid Jacobian operators

The non-inherited and the inherited version (denoted with superscript \mathcal{I}) of the inviscid and viscous Jacobian operators introduced in (10)-(11), can be defined as follows for $\ell = 1, \dots, L$

$$\begin{aligned}
(\mathbf{J}_\ell^{1v} \delta \mathbf{w}_h, \mathbf{z}_h)_{L^2(\Omega)} &= j_h^{1v}(\mathbf{w}_h, \delta \mathbf{w}_h, \mathbf{z}_h) & \forall \mathbf{w}_h, \delta \mathbf{w}_h, \mathbf{z}_h \in [\mathbb{P}_d^{\kappa_\ell}(\mathcal{T}_h)]^{d+1} \\
(\mathbf{J}_\ell^v \delta \mathbf{w}_h, \mathbf{z}_h)_{L^2(\Omega)} &= j_h^v(\delta \mathbf{w}_h, \mathbf{z}_h) & \forall \delta \mathbf{w}_h, \mathbf{z}_h \in [\mathbb{P}_d^{\kappa_\ell}(\mathcal{T}_h)]^{d+1} \\
(\mathbf{J}_\ell^{1v, \mathcal{I}} \delta \mathbf{w}_h, \mathbf{z}_h)_{L^2(\Omega)} &= j_h^{1v}(\mathbf{w}_h, \mathcal{I}_\ell^0 \delta \mathbf{w}_h, \mathcal{I}_\ell^0 \mathbf{z}_h) & \forall \mathbf{w}_h, \delta \mathbf{w}_h, \mathbf{z}_h \in [\mathbb{P}_d^{\kappa_\ell}(\mathcal{T}_h)]^{d+1} \\
(\mathbf{J}_\ell^{v, \mathcal{I}} \delta \mathbf{w}_h, \mathbf{z}_h)_{L^2(\Omega)} &= j_h^v(\mathcal{I}_\ell^0 \delta \mathbf{w}_h, \mathcal{I}_\ell^0 \mathbf{z}_h) & \forall \delta \mathbf{w}_h, \mathbf{z}_h \in [\mathbb{P}_d^{\kappa_\ell}(\mathcal{T}_h)]^{d+1}
\end{aligned} \tag{18}$$

The main benefit of inherited algorithms is the possibility to efficiently compute coarse grid operators by means of the so called Galerkin projection, avoiding the cost of assembling bilinear and trilinear forms. The procedure is described in what follows, focusing on the benefits of using hierarchical orthonormal basis functions.

The matrix counterpart $\mathbf{J}_\ell^{\mathcal{I}}$ of the operator $\mathbf{J}_\ell^{\mathcal{I}} = \mathbf{J}_\ell^{v, \mathcal{I}} + \mathbf{J}_\ell^{1v, \mathcal{I}}$ is a sparse block matrix with block dimension $N_{\text{dof}}^\kappa = \dim(\mathbb{P}_d^{\kappa}(\kappa))$ and total dimension $\text{card}(\mathcal{T}_h) N_{\text{dof}}^\kappa (d+1)$. The matrix is composed of diagonal blocks $\mathbf{J}_{\kappa, \kappa}^{\ell, \mathcal{I}}$ and off-diagonal blocks $\mathbf{J}_{\kappa, \kappa'}^{\ell, \mathcal{I}}$, the latter taking care of the coupling between neighboring elements κ, κ' sharing a face σ . Once the fine system matrix \mathbf{J}_0 is assembled, the diagonal and off-diagonal blocks of the Jacobian matrix of coarse levels can be inherited recursively and matrix-free as follows

$$\mathbf{J}_{\kappa, \kappa}^{\ell+1, \mathcal{I}} = \mathbf{M}_{\ell+1, \ell}^\kappa \left(\mathbf{J}_{\kappa, \kappa}^{\ell, \mathcal{I}} \right) \left(\mathbf{M}_{\ell+1, \ell}^\kappa \right)^t, \quad \mathbf{J}_{\kappa, \kappa'}^{\ell+1, \mathcal{I}} = \mathbf{M}_{\ell+1, \ell}^\kappa \left(\mathbf{J}_{\kappa, \kappa'}^{\ell, \mathcal{I}} \right) \left(\mathbf{M}_{\ell+1, \ell}^{\kappa'} \right)^t. \tag{19}$$

The projection matrices read

$$\mathbf{M}_{\ell+1, \ell}^\kappa = \left(\mathbf{M}_{\ell+1}^\kappa \right)^{-1} \int_\kappa \varphi^{\ell+1} \otimes \varphi^\ell, \quad \text{where} \quad \mathbf{M}_{\ell+1}^\kappa = \int_\kappa \varphi^{\ell+1} \otimes \varphi^{\ell+1}, \tag{20}$$

and φ^ℓ represents the set of basis functions spanning the space $\mathbb{P}_d^{\kappa_\ell}(\kappa)$. When using hierarchical orthonormal basis functions, $\mathbf{M}_{\ell+1}^\kappa$ is the unit diagonal elemental mass matrix and $\mathbf{M}_{\ell+1, \ell}^\kappa \in \mathbb{R}^{\dim(\mathbb{P}_d^{\kappa_{\ell+1}}(\kappa)) \times \dim(\mathbb{P}_d^{\kappa_\ell}(\kappa))}$ is a unit diagonal rectangular matrix. Accordingly the Galerkin projection in (19) falls back to a trivial and inexpensive sub-block extraction.

Being $\mathbb{P}_d^{k_0}(\mathcal{T}_h) \supset \mathbb{P}_d^{\kappa_\ell}(\mathcal{T}_h)$, it can be demonstrated that inherited and non-inherited p -multigrid algorithms lead to the same inviscid Jacobian operators, that is $\mathbf{J}_\ell^{1v, \mathcal{I}} = \mathbf{J}_\ell^{1v}$. As opposite inherited and non-inherited viscous Jacobian differ because of the terms involving lifting operators. Note that inherited lifting operators act on traces of polynomial functions mapped into $\mathbb{P}_d^{k_0}(\mathcal{T}_h)$, accordingly

$$\text{inherited } p\text{-multigrid lifting operators, } \mathbf{r}^\sigma(\llbracket z_h \rrbracket) : \mathbb{P}_d^{k_0}(\sigma) \rightarrow [\mathbb{P}_d^{k_0}(\mathcal{T}_h)]^d, \tag{21}$$

$$\text{non-inherited } p\text{-multigrid lifting operators, } \mathbf{r}^\sigma(\llbracket z_h \rrbracket) : \mathbb{P}_d^{\kappa_\ell}(\sigma) \rightarrow [\mathbb{P}_d^{\kappa_\ell}(\mathcal{T}_h)]^d. \tag{22}$$

Interestingly, using the definitions of the global and local lifting operators, the bilinear form

can be rewritten as follows

$$\begin{aligned}
j_h^v(\delta w_h, z_h) = & - \sum_{\kappa \in \mathcal{F}_h} \int_{\kappa} \sum_{i,j=1}^d \sum_{p,q=1}^d \frac{\partial \widehat{F}_{p,i}}{\partial (\partial w_j / \partial x_q - R_q^\kappa(w_j))} \frac{\partial (\delta w_j)}{\partial x_q} \frac{\partial z_i}{\partial x_p} + \\
& + \sum_{\sigma \in \mathcal{F}_h} \int_{\sigma} \sum_{i,j=1}^d \sum_{p,q=1}^d n_q^\sigma \frac{\partial \widehat{F}_{p,i}}{\partial (\partial w_j / \partial x_q - R_q^\kappa(w_j))} \llbracket \delta w_j \rrbracket \left\{ \left\{ \frac{\partial z_i}{\partial x_p} \right\} \right\} + \\
& + \sum_{\sigma \in \mathcal{F}_h} \int_{\sigma} \sum_{i,j=1}^d \sum_{p,q=1}^d n_p^\sigma \frac{\partial \widehat{F}_{p,i}}{\partial (\partial w_j / \partial x_q - \eta_\sigma r_q^\sigma(w_j))} \left\{ \left\{ \frac{\partial (\delta w_j)}{\partial x_q} \right\} \right\} \llbracket z_i \rrbracket + \\
& - \sum_{\sigma \in \mathcal{F}_h} \int_{\Omega} \sum_{i,j=1}^d \sum_{p,q=1}^d \eta_\sigma \frac{\partial \widehat{F}_{p,i}}{\partial (\partial w_j / \partial x_q - \eta_\sigma r_q^\sigma(w_j))} r_q^\sigma (\llbracket \delta w_j \rrbracket) r_p^\sigma (\llbracket z_i \rrbracket) \quad (23)
\end{aligned}$$

showing that only the last term, *i.e.*, the stabilization term, cannot be reformulated lifting-free. In particular, as will be demonstrated in the following section, the inherited stabilization term introduces an excessive amount of stabilization with respect to its non-inherited counterpart, which is detrimental for multigrid algorithm performance. The same behaviour was previously documented in the context of h -multigrid solution strategies, see [20] where the authors consider dG discretizations of the INS equations and [26], where preconditioners for weakly over-penalized symmetric interior penalty dG discretization of elliptic problems are devised.

2.4.1. Scaling of the stabilization term

Following the idea proposed by [20] we consider the possibility to introduce a rescaled Galerkin projection of the stabilization term in order to recover the optimal performances of non-inherited p -multigrid algorithm.

As a first point we recall the following bound on the local lifting operator: let $\phi \in L^2(\sigma)$, for all $\sigma \in \mathcal{F}_h$

$$\|\mathbf{r}_\sigma^k(\phi)\|_{[L^2(\Omega)]^d} \leq C_{tr} h_{\kappa,\kappa'}^{-1/2} \|\phi\|_{L^2(\sigma)}, \quad (24)$$

where $h_{\kappa,\kappa'} = \min(h_\kappa, h_{\kappa'})$, see *e.g.* [27, Lemma 2], [28, Lemma 7.2] or [29, Lemma 4.33 and Lemma 5.18] for a proof. The constant C_{tr} depends on d, k and the shape regularity of the elements sharing σ and is inherited from the discrete trace inequality: for all $\kappa \in \mathcal{T}_h, \sigma \in \mathcal{F}_h$

$$\|z_h\|_{L^2(\sigma)} \leq C_{tr} h_{\kappa,\kappa'}^{-1/2} \|z_h\|_{L^2(\kappa)} \quad (25)$$

As remarked by Di Pietro and Ern [29, Lemma 1.46] the dependence of C_{tr} on k is a delicate issue that has a precise answer only in specific cases. In this work we follow the estimates given by Hesthaven and Warburton [30] showing that for simplicial meshes C_{tr} scales as $\sqrt{k(k+d)}$ when using complete polynomials of maximum degree k . This choice turns out to be conservative regarding the dependence on k with respect to estimates derived by Schwab [31] based on tensor product polynomials on mesh elements being affine images of the unit hypercube in \mathbb{R}^d , which suggest a $\sqrt{k(k+1)}$ scaling.

Using the Cauchy-Schwarz inequality, for all $\mathbf{w}_h, \mathbf{z}_h \in [\mathbb{P}_d^k(\mathcal{T}_h)]^{d+1}$ we get

$$\begin{aligned} j_h^{\nu\text{-STB}}(\mathbf{w}_h, \mathbf{z}_h)|_{\sigma \in \mathcal{F}_h} &= \eta_\sigma \int_\Omega \sum_{i,j=1}^d \sum_{p,q=1}^d \frac{\partial \widehat{F}_{p,i}}{\partial (\partial w_j / \partial x_q - \eta_\sigma r_q^\sigma(w_j))} \mathbf{r}_q^\sigma(\llbracket w_j \rrbracket) \mathbf{r}_p^\sigma(\llbracket v_i \rrbracket) \\ &\leq \eta_\sigma C k_\ell (k_\ell + d) h_{\kappa, \kappa'}^{-1} \|\llbracket \mathbf{w}_h \rrbracket\|_{L^2(\sigma)} \|\llbracket \mathbf{v}_h \rrbracket\|_{L^2(\sigma)} \\ j_h^{\nu\text{-STB}}(\mathcal{I}_\ell^0 \mathbf{w}_h, \mathcal{I}_\ell^0 \mathbf{z}_h)|_{\sigma \in \mathcal{F}_h} &= \eta_\sigma \int_\Omega \sum_{i,j=1}^d \sum_{p,q=1}^d \frac{\partial \widehat{F}_{p,i}}{\partial (\partial w_j / \partial x_q - \eta_\sigma r_q^\sigma(w_j))} \mathbf{r}_q^\sigma(\llbracket w_j \rrbracket) \cdot \mathbf{r}_p^\sigma(\llbracket v_i \rrbracket) \\ &\leq \eta_\sigma C k_0 (k_0 + d) h_{\kappa, \kappa'}^{-1} \|\llbracket \mathbf{w} \rrbracket\|_{L^2(\sigma)} \|\llbracket \mathbf{v} \rrbracket\|_{L^2(\sigma)} \end{aligned}$$

where C is independent from h and k . As a result we are able to introduce the scaling factor $\mathcal{S}_0^\ell = \frac{(k_\ell)(k_\ell+d)}{(k_0)(k_0+d)}$ such that, for all $\mathbf{w}_h, \mathbf{z}_h \in [\mathbb{P}_d^k(\mathcal{T}_h)]^{d+1}$, it holds

$$j_h^{\nu\text{-STB}}(\mathbf{w}_h, \mathbf{z}_h) \simeq \mathcal{S}_0^\ell j_h^{\nu\text{-STB}}(\mathcal{I}_\ell^0 \mathbf{w}_h, \mathcal{I}_\ell^0 \mathbf{z}_h). \quad (26)$$

The viscous Jacobian stabilization operator reads

$$(\mathbf{J}_\ell^{\nu\text{-STB}}(\delta \mathbf{w}_h), \mathbf{z}_h)_{L^2(\Omega)} = \mathcal{S}_0^\ell j_h^{\nu\text{-STB}}(\mathcal{I}_\ell^0(\delta \mathbf{w}_h), \mathcal{I}_\ell^0 \mathbf{z}_h) \quad \forall \delta \mathbf{w}_h, \mathbf{z}_h \in [\mathbb{P}_d^{k_\ell}(\mathcal{T}_h)]^{d+1} \quad (27)$$

and, accordingly, the Jacobian stabilization diagonal and off-diagonal block contributions $\mathbf{J}_{\kappa, \kappa}^{\ell, \nu\text{-STB}, \mathcal{I}}$ and $\mathbf{J}_{\kappa, \kappa'}^{\ell, \nu\text{-STB}, \mathcal{I}}$ can be computed recursively and matrix free by means of a rescaled Galerkin projection. The rescaled-inherited blocks of the Jacobian matrix are computed as follows

$$\mathbf{J}_{\kappa, \kappa}^{\ell+1, \mathcal{I}} = \mathbf{M}_{\ell+1, \ell}^\kappa \left(\mathbf{J}_{\kappa, \kappa}^{\ell, \nu, \nu \setminus \text{STB}, \mathcal{I}} \right) \left(\mathbf{M}_{\ell+1, \ell}^{\kappa'} \right)^t + \mathcal{S}_\ell^{\ell+1} \mathbf{M}_{\ell+1, \ell}^\kappa \left(\mathbf{J}_{\kappa, \kappa}^{\ell, \nu\text{-STB}, \mathcal{I}} \right) \left(\mathbf{M}_{\ell+1, \ell}^{\kappa'} \right)^t, \quad (28)$$

$$\mathbf{J}_{\kappa, \kappa'}^{\ell+1, \mathcal{I}} = \mathbf{M}_{\ell+1, \ell}^\kappa \left(\mathbf{J}_{\kappa, \kappa'}^{\ell, \nu, \nu \setminus \text{STB}, \mathcal{I}} \right) \left(\mathbf{M}_{\ell+1, \ell}^{\kappa'} \right)^t + \mathcal{S}_\ell^{\ell+1} \mathbf{M}_{\ell+1, \ell}^\kappa \left(\mathbf{J}_{\kappa, \kappa'}^{\ell, \nu\text{-STB}, \mathcal{I}} \right) \left(\mathbf{M}_{\ell+1, \ell}^{\kappa'} \right)^t, \quad (29)$$

where $\mathcal{S}_\ell^{\ell+1} = \frac{(k_{\ell+1})(k_{\ell+1}+d)}{(k_\ell)(k_\ell+d)}$. We remark that $\mathbf{J}_{\kappa, \kappa}^{\ell, \nu, \nu \setminus \text{STB}}$ and $\mathbf{J}_{\kappa, \kappa'}^{\ell, \nu, \nu \setminus \text{STB}}$ are the Jacobian blocks corresponding to inviscid contributions plus the viscous contributions without the stabilization terms.

2.4.2. The p -multigrid iteration

In this section we provide an overlook of the sequence of operations involved in p -multigrid iterations. The recursive p -multigrid \mathcal{V} -cycle and full p -multigrid \mathcal{V} -cycle for the problem $\mathbf{G}_\ell \delta \mathbf{w}_\ell = \mathbf{g}_\ell$ on level ℓ reads:

Algorithm 2 $\bar{\mathbf{w}}_\ell = \text{MG}_{\mathcal{V}}(l, \mathbf{g}_\ell, \mathbf{w}_\ell)$

```
if ( $\ell = L$ ) then
   $\bar{\mathbf{w}}_\ell = \text{SOLVE}(\mathbf{G}_\ell, \mathbf{g}_\ell, 0)$ 
end if
if ( $\ell < L$ ) then
  Pre-smoothing:
   $\bar{\mathbf{w}}_\ell = \text{SMOOTH}(\mathbf{G}_\ell, \mathbf{g}_\ell, \mathbf{w}_\ell)$ 

  Coarse grid correction:
   $\mathbf{d}_\ell = \mathbf{g}_\ell - \mathbf{G}_\ell \bar{\mathbf{w}}_\ell$ 
   $\mathbf{d}_{\ell+1} = \mathcal{I}_\ell^{\ell+1} \mathbf{d}_\ell$ 
   $\mathbf{e}_{\ell+1} = \text{MG}_{\mathcal{V}}(\ell + 1, \mathbf{d}_{\ell+1}, 0)$ 
   $\widehat{\mathbf{w}}_\ell = \bar{\mathbf{w}}_\ell + \mathcal{I}_{\ell+1}^\ell \mathbf{e}_{\ell+1}$ 

  Post-smoothing:
   $\bar{\mathbf{w}}_\ell = \text{SMOOTH}(\mathbf{G}_\ell, \mathbf{g}_\ell, \widehat{\mathbf{w}}_\ell)$ 
end if
return  $\bar{\mathbf{w}}_\ell$ 
```

Algorithm 3 $\bar{\mathbf{w}}_\ell = \text{MG}_{\text{full}}(l, \mathbf{g}_\ell, \mathbf{w}_\ell)$

```
if ( $\ell = L$ ) then
   $\bar{\mathbf{w}}_\ell = \text{SOLVE}(\mathbf{G}_\ell, \mathbf{g}_\ell, 0)$ 
end if
if ( $\ell < L$ ) then
   $\mathbf{g}_{\ell+1} = \mathcal{I}_\ell^{\ell+1} \mathbf{g}_\ell$ 
   $\widehat{\mathbf{w}}_{\ell+1} = \text{MG}_{\text{full}}(\ell + 1, \mathbf{g}_{\ell+1}, 0)$ 
   $\mathcal{V}$ -cycle correction:
   $\widehat{\mathbf{w}}_\ell = \mathcal{I}_{\ell+1}^\ell \widehat{\mathbf{w}}_{\ell+1}$ 
   $\mathbf{d}_\ell = \mathbf{g}_\ell - \mathbf{G}_\ell \widehat{\mathbf{w}}_\ell$ 
   $\mathbf{e}_\ell = \text{MG}_{\mathcal{V}}(\ell, \mathbf{d}_\ell, 0)$ 
   $\bar{\mathbf{w}}_\ell = \widehat{\mathbf{w}}_\ell + \mathbf{e}_\ell$ 
end if
return  $\bar{\mathbf{w}}_\ell$ 
```

To obtain an application of the p -multigrid preconditioner the multilevel iteration is invoked on the problem $\mathbf{G}_h \delta \mathbf{w}_h = \mathbf{g}_h$. While one $\text{MG}_{\mathcal{V}}$ iteration requires two applications of the smoother on the finest level (one pre- and one post-smoothing) and one application of the coarse level smoother independently from the number of levels, one MG_{full} iteration requires one application of the finest level smoother and L applications of the coarse level smoother.

In this work the p -multigrid \mathcal{V} cycle iteration will be applied for the numerical solution of Poisson problems while the full p -multigrid iteration will be applied for the solution of linearized equations systems arising in Rosenbrock time marching strategies for dG discretizations of incompressible flow problems. In the context of Poisson problems we apply the most simple multigrid solution strategy with a single smoothing iteration on all levels except the coarsest for validation purposes. In the context of incompressible flow problem we seek for the best performance employing full p -multigrid and tuning preconditioners and smoothing options.

2.4.3. Matrix-free and matrix-based preconditioned iterative solution strategies

In this work, for the sake of comparison, we consider several multigrid and single-grid preconditioner strategies for Krylov iterative solvers with application to the solution of linear system arising in Rosenbrock-type schemes, see Eq. (13). For the sake of compactness, a solver-preconditioner couple is identify by the following naming convention:

SOLVER(MatrixVectorProdOptions)[PRECONDITIONER(PreconditionerOptions)].

The MatrixVectorProdOptions describes how matrix-vector products need by Krylov iterative solvers, see *e.g.* [32], are performed, there are two possibilities:

- i) Matrix-Based (MB) where the action of the matrix on the defect vector requires to explicitly assemble the entries of the global system matrix;
- ii) Matrix-Free (MF) where the action of the matrix on the defect vector is approximated by means of a first order Taylor expansion, see *e.g.*, [33].

For example, in a matrix-free framework, given $\mathbf{w}_h, \mathbf{d}_h \in [\mathbb{P}_d^{\kappa_\ell}(\mathcal{T}_h)]^{d+1}$ the Jacobian trilinear form can be approximated by evaluating twice the residual bilinear form, as follows

$$j_h(\mathbf{w}_h^n, \mathbf{d}_h, \mathbf{z}_h) = \frac{1}{\Delta} \left(f(\mathbf{w}_h^n + \Delta \mathbf{d}_h, \mathbf{z}_h) - f(\mathbf{w}_h^n, \mathbf{z}_h) \right), \quad \forall \mathbf{z}_h \in [\mathbb{P}_d^{\kappa_\ell}(\mathcal{T}_h)]^{d+1}, \quad (30)$$

where, according to [34],

$$\Delta = \epsilon \frac{\sqrt{1 + \|\mathbf{w}_h^n\|_{L^2(\Omega)}}}{\|\mathbf{d}_h\|_{L^2(\Omega)}}, \quad (31)$$

with $\epsilon = 10^{-9}$ for all the computations [35, 11, 10]. Since the global system matrix is not stored in memory, the Jacobian matrix can be assembled for preconditioning purposes only resulting in a less memory-demanding implementation. Depending on the preconditioner strategy also the assembly costs can be reduced, for example by evaluating only parts of the Jacobian blocks, and/or reusing those blocks for several successive iterations.

GMRES and FGMRES solvers are employed in combination with single-grid and p -multigrid preconditioners, respectively, we remark that also p -multigrid iterations rely on GMRES preconditioned iterative solver for smoothing purposes. As preconditioners for GMRES iterations we consider the following options:

1. ASM(i,ILU(j)) - Additive Schwarz domain decomposition Method (ASM) preconditioners with i levels of overlap between sub-domains and a block ILU decomposition for each sub-domain matrix with j levels of fill;
2. BJ or ASM(0,ILU(0)) - ASM preconditioner with no overlap between sub-domains and a block ILU decomposition for each sub-domain matrix with same level of fill of the original matrix;
3. EWBJ - Element Wise Block Jacobi, a BJ preconditioner neglecting off-diagonal blocks, that is an LU factorization of the diagonal blocks.

Note that in serial computations ASM(i,ILU(j)) and BJ fall back to ILU(j) and ILU(0), respectively. ASM and BJ performance differ when the computation is performed in parallel, depending on the number of sub-domains. While efficiency of BJ decreases while increasing the number of sub-domains, ASM seek to heal the convergence degradation at the expense of an increased memory footprint of the solver as the number of partitions rise (indeed part of the global matrix non-zeros entries are replicated in neighboring sub-domains). As opposite EWBJ has optimal scalability properties and is particularly well suited for a matrix-free implementation of the iterative solver. Indeed, in this context, it allows to skip the computation of the off-diagonal contributions, thereby reducing the matrix-assembly computation time.

As smoother's preconditioners EWBJ is particularly well suited on the finest level, for the sake of reducing the memory footprint, while ASM makes sense on the coarsest level, to improve the convergence rate of the coarse solver. In this configuration, the off-diagonal blocks needed by the coarsest level operator can be computed at the coarsest polynomial degree for the sake of efficiency. In the rest of the paper several combinations of preconditioners are investigated with particular attention to the quantification of the parallel performance and of the memory savings. The code relies on the PETSc library to handle linear solvers and parallelism [36].

2.5. Memory footprint considerations

In this section an estimate of the memory footprint of all the strategies employed in this paper is devised to fully appreciate the memory savings achievable through a matrix-free solver preconditioned with p -multigrid. We observe that the memory footprint of the global block matrix scales as

$$\text{card}(\mathcal{T}_h) \overline{\text{card}(\mathcal{F}_{\partial\kappa})} + 1 \left((d+1) \dim(\mathbb{P}_d^k) \right)^2,$$

where $\overline{\text{card}(\mathcal{F}_{\partial\kappa})}$ is the average number of element's faces, $d+1$ is the number of variables in d space dimensions and $\left((d+1) \dim(\mathbb{P}_d^k) \right)^2$ is the number of non-zeros in each matrix block. While for a matrix-based implementation we assume that both the global system matrix and the preconditioner are stored in memory, for a matrix-free approach only the preconditioner is stored. The preconditioner's memory footprint is carefully estimated:

1. for EWBJ, we consider only the non-zero entries of a block-diagonal matrix.
2. For BJ we consider the storage of ILU(0) factorization applied to the domain-wise portion of the iteration matrix, which neglects the off diagonal blocks related to faces residing on a partition boundary.
3. For ASM(q ,ILU(0)), we assume that the preconditioner applies the ILU(0) decomposition to a larger matrix, bigger than the sub-domain matrix of the BJ preconditioner. The exact number of additional non-zero blocks is difficult to estimate for general unstructured grids since it depends on mesh topology, element types (in case of hybrid grids) and the partitioning strategy. Nevertheless, an estimation can be done based on the following simplifications: we assume a square and cubical domain discretized by uniformly distributed quadrilateral and hexahedral elements in $2d$ and $3d$, respectively, and we consider periodic boundary conditions on the domain boundaries. Accordingly the number of non-zero blocks in each sub-domain matrix can be estimated as follows

$$(2d+1) \left(\frac{N_e}{p} + 2dq \left(\frac{N_e}{p} \right)^{\frac{d-1}{d}} + 2^{d-1} d \sum_{i=1}^q (i-1) \right) - 2d \left(\left(\left(\frac{N_e}{p} \right)^{\frac{1}{d}} + 2q \right)^{d-1} - 2^{d-1} (d-2) \sum_{i=0}^q (q-i) \right) \quad (32)$$

where q is the number (or depth) of overlapping layers, p is the number of processes, $N_e = \text{card}(\mathcal{T}_h)$ is the number of mesh elements and $\overline{\text{card}(\mathcal{F}_{\partial\kappa})} = 2d$. In Eq. (32), the first term takes into account that each element of a partition, which is widened with the overlapping elements, contributes to the Jacobian matrix with $(1+2d)$ blocks, being $2d$ the number of faces of an element, while the second term subtracts the blocks not considered by the preconditioner, being they due to connection between elements at the boundary faces of the augmented partition. For $q = \{0, 1, 2\}$ we get an estimation of the number of non-zero blocks corresponding to BJ, ASM(1,ILU(0)) and ASM(2,ILU(0)) preconditioners, respectively. The number of non-zero entries of the global matrix can be obtained multiplying by the number of non-zeros in each block.

Figures 1(a) and 1(b) report the ratio between the estimated number of non-zeros of the preconditioner and the system matrix with respect to the number of sub-domains. For $(N_e/p) = 1$, corresponding to one element per partition, BJ reduces to EWBJ, which provides a $1/(2d+1)$ decrease of the number of non-zeros. On the other hand, for both ASM(1,ILU(0)) and ASM(2,ILU(0)) the number of non-zero entries grows as (N_e/p) approaches one. In the same manner the memory

footprint of p -multigrid preconditioners can be estimated. We consider as reference the three-level p -multigrid strategy whose specs, also reported on top of Table 8, reads: $k = 6$, FGMRES(MF) outer solver, GMRES(MB)[ASM(1,ILU(0))] smoothing on the coarsest level ($k = 1$), GMRES(MF)[EWBJ] on the finest level ($k = 6$) and GMRES(MB)[EWBJ] on the intermediate level ($k = 2$). We remark that the memory allocation of coarse levels preconditioners has as a small impact on the total number of non-zeros, due the reduction of block size. For instance, in three space dimensions, \mathbf{G}_2 and \mathbf{G}_1 have 440 and 70 time less non-zeros that the \mathbf{G}_0 matrix, respectively.

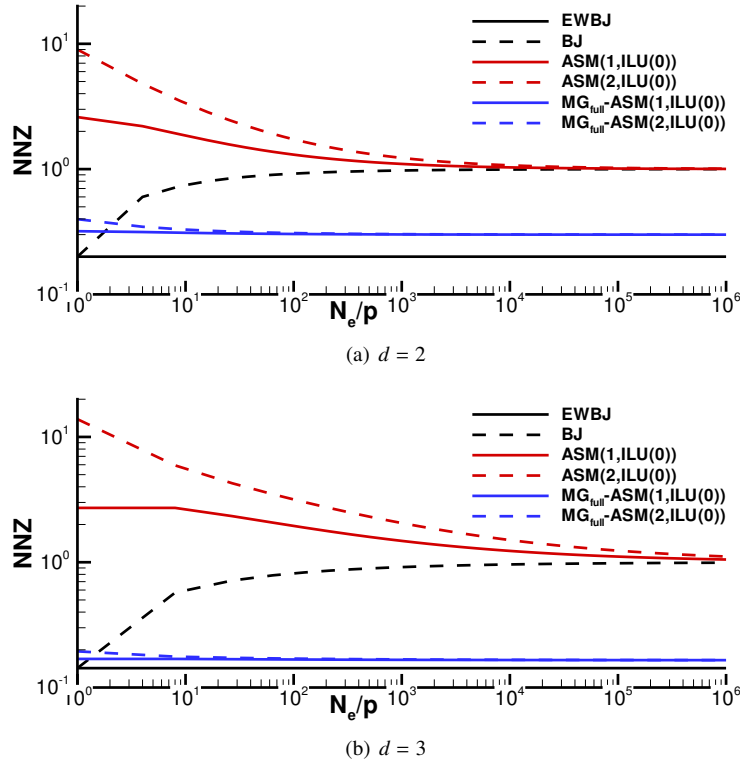


Figure 1: Estimated relative number of non-zeros (NNZ) of the preconditioner with respect to the non-zeros of the Jacobian as a function of the number of elements per partition for a two dimensional ($d = 2$) and three-dimensional case ($d = 3$). See text for details.

3. Numerical results

3.1. Assessment of the stabilization scaling on a Poisson Problem

Since the stabilization scaling influences only the elliptic part of coarse grid operators, it makes sense to assess its effectiveness tackling the numerical solution of a Poisson problem. In particular we consider the performance of a p -multigrid preconditioned FMGRES solver applied to a high-order $k = 6$ BR2 dG discretization over three h -refined mesh sequences of the bi-unit square $\Omega = [-1, 1]^2$: i) a regular Delaunay triangular mesh sequence (reg-tri), ii) a distorted quadrilateral

mesh sequence (dist-quad) obtained by randomly perturbing the nodes of a Cartesian grid, iii) a distorted and graded triangular mesh sequence (grad-tri) where the elements shrink close to the domain boundaries mimicking the end-points clustering of one-dimensional Gaussian quadrature rules in each Cartesian direction. Dirichlet boundary conditions and the forcing term are imposed according to the smooth exact solution $u = e^{-2.5((x-1)^2+(y-1)^2)}$. The potential field rapidly varies in the proximity of the upper-right corner of the square in order to replicate the presence of a boundary layer.

The p -multigrid preconditioner options are as follows: we consider a three-levels ($L = 2$) and a six-levels ($L = 5$) \mathcal{V} -cycle iteration with ILU(0) right-preconditioned GMRES smoothers on each level. On all levels but the coarsest (that is for $\ell < L$) we perform a single smoothing iteration. On the coarse level we set the relative residual tolerance to 10^{-3} and impose a maximum number of iterations of 40 or 400. Polynomial degree coarsening on six-levels is achieved by recursively reducing the polynomial degree by one, that is $\kappa_\ell = 6 - \ell$. On three the coarsening strategy is more aggressive: we drop to $k=3$ on the first level and we employ a second-order $k=1$ dG discretization on the coarsest level. Interestingly, this latter setup seeks to replicate the four-fold degrees of freedom decrease of h -multigrid strategies in two space dimensions.

In Table 1 and Table 2 we consider the three- and the six-levels \mathcal{V} -cycle iterations, respectively, and we assess the benefits of stabilization scaling (scaling on) with respect to standard inherited- p -multigrid coarse grid operators (scaling off). Execution time gains are remarkable on regular triangular and distorted quadrilateral mesh sequences (solution time speedup of 2.4 and 2.2 on average, respectively) but still present on the graded triangular mesh sequence (50% faster solution process on average).

Performance of iterative solver can be evaluated in terms of convergence factor, that is the average residual decrease per iteration, which can be computed as follows

$$\rho = e^{\left(\frac{1}{N_{it}} \ln \frac{\|d_{N_{it}}\|}{\|d_0\|}\right)},$$

where N_{it} is the number of iterations required to reach the prescribed residual drop, and d_i is the defect (or residual) of the linear system solution at the i -th iteration. It is interesting to remark that stabilization scaling always improves the convergence factor of the coarse grid solver having a positive impact on the performance of the algorithm, in particular one of two following situations might occur.

1. The prescribed residual drop of 10^{-3} is attained in a smaller number of coarse solver iterations. This is typically observed when the maximum number of iterations is set to 400.
2. The prescribed maximum number of iteration of the coarse solver is attained leading to a tinier defect for the rescaled stabilization algorithm. Accordingly, convergence of the outer solver is improved and a smaller number of FGMRES iterations is required to solve the linear system. This is typically observed when the maximum number of iterations of the coarse solver is set to 40.

We remark that uniform convergence with respect to the mesh density is obtained on regular triangular and distorted quadrilateral mesh sequences when employing a sufficiently high number of GMRES iterations on the coarse level. On the distorted and graded triangular mesh sequence the number of FGMRES iterations increases with the mesh density due to the presence of increasingly stretched elements close to the domain boundaries. Note that the number of iteration

increase is less pronounced when employing six-levels instead of three-levels for the \mathcal{V} -cycle iteration.

To conclude, we mention that the number of iterations of rescaled-inherited and non-inherited multigrid has been checked to be equal on all but the finest grids of the distorted and graded triangular mesh sequence, where the former is slightly sub-optimal as compared to the latter (by at most 20%). This confirms that stabilization terms scaling is almost able to recover the convergence rates of non-inherited multigrid while also cutting down assembly costs.

| | Solver | | ℓ | κ_ℓ | rTol | ITs | Smoother | | | |
|---------------------|----------------------------|----------|--------|---------------|------------|----------|---------------|----------|---------|------|
| | | | 0 | 6 | – | 1 | | | | |
| | FGMRES[MG ν], $L = 2$ | | 1 | 3 | – | 1 | GMRES[ILU(0)] | | | |
| | | | 2 | 1 | 10^{-3} | 400 | | | | |
| grid | scaling off | | | | scaling on | | | | speedup | |
| reg-tri | ρ | ρ_c | ITs | ITs $_c$ | ρ | ρ_c | ITs | ITs $_c$ | Tot | Sol |
| 39 ² ·2 | 0.0822 | 0.957 | 10 | 157 | 0.112 | 0.833 | 11 | 38 | 1.3 | 1.7 |
| 79 ² ·2 | 0.0711 | 0.969 | 9 | 223 | 0.108 | 0.929 | 11 | 95 | 1.7 | 2.3 |
| 158 ² ·2 | 0.0847 | 0.99 | 10 | 399 | 0.117 | 0.946 | 11 | 125 | 2 | 2.5 |
| 311 ² ·2 | 0.133 | 0.997 | 12 | 399 | 0.107 | 0.982 | 11 | 385 | 1.2 | 1.2 |
| dist-quad | ρ | ρ_c | ITs | ITs $_c$ | ρ | ρ_c | ITs | ITs $_c$ | Tot | Sol |
| 32 ² | 0.0718 | 0.913 | 9 | 76 | 0.0409 | 0.764 | 8 | 26 | 1.2 | 1.5 |
| 64 ² | 0.0694 | 0.956 | 9 | 155 | 0.0405 | 0.865 | 8 | 48 | 1.4 | 2 |
| 128 ² | 0.0641 | 0.966 | 9 | 200 | 0.0369 | 0.881 | 7 | 55 | 1.9 | 3.3 |
| 256 ² | 0.0606 | 0.989 | 9 | 399 | 0.0279 | 0.957 | 7 | 159 | 2.1 | 3 |
| grad-tri | ρ | ρ_c | ITs | ITs $_c$ | ρ | ρ_c | ITs | ITs $_c$ | Tot | Sol |
| 32 ² ·2 | 0.141 | 0.909 | 12 | 73 | 0.165 | 0.747 | 13 | 24 | 1.1 | 1.1 |
| 64 ² ·2 | 0.204 | 0.929 | 15 | 94 | 0.214 | 0.774 | 15 | 27 | 1.2 | 1.4 |
| 128 ² ·2 | 0.285 | 0.96 | 19 | 170 | 0.315 | 0.925 | 20 | 89 | 1.5 | 1.8 |
| 256 ² ·2 | 0.359 | 0.965 | 23 | 194 | 0.436 | 0.944 | 28 | 120 | 1.3 | 1.4 |
| | Solver | | ℓ | κ_ℓ | rTol | ITs | Smoother | | | |
| | | | 0 | 6 | – | 1 | | | | |
| | FGMRES[MG ν], $L = 2$ | | 1 | 3 | – | 1 | GMRES[ILU(0)] | | | |
| | | | 2 | 1 | 10^{-3} | 40 | | | | |
| grid | scaling off | | | | scaling on | | | | speedup | |
| reg-tri | ρ | ρ_c | ITs | ITs $_c$ | ρ | ρ_c | ITs | ITs $_c$ | Tot | Sol |
| 39 ² ·2 | 0.194 | 0.962 | 15 | 39 | 0.112 | 0.909 | 11 | 39 | 1.1 | 1.3 |
| 79 ² ·2 | 0.356 | 0.983 | 23 | 39 | 0.142 | 0.954 | 12 | 39 | 1.4 | 1.8 |
| 158 ² ·2 | 0.665 | 0.993 | 56 | 39 | 0.226 | 0.985 | 16 | 39 | 2.2 | 3.2 |
| 311 ² ·2 | 0.819 | 0.994 | 113 | 39 | 0.408 | 0.986 | 26 | 39 | 3.1 | 4.1 |
| dist-quad | ρ | ρ_c | ITs | ITs $_c$ | ρ | ρ_c | ITs | ITs $_c$ | Tot | Sol |
| 32 ² | 0.0939 | 0.962 | 10 | 39 | 0.0409 | 0.72 | 8 | 21 | 1.1 | 1.3 |
| 64 ² | 0.162 | 0.982 | 13 | 39 | 0.0406 | 0.877 | 8 | 39 | 1.2 | 1.5 |
| 128 ² | 0.351 | 0.976 | 23 | 39 | 0.0669 | 0.958 | 9 | 39 | 1.5 | 2.3 |
| 256 ² | 0.621 | 0.993 | 48 | 39 | 0.148 | 0.958 | 13 | 39 | 2.2 | 3.3 |
| grad-tri | ρ | ρ_c | ITs | ITs $_c$ | ρ | ρ_c | ITs | ITs $_c$ | Tot | Sol |
| 32 ² ·2 | 0.146 | 0.898 | 12 | 39 | 0.164 | 0.765 | 13 | 26 | 0.99 | 0.99 |
| 64 ² ·2 | 0.215 | 0.971 | 15 | 39 | 0.214 | 0.867 | 15 | 39 | 1 | 1 |
| 128 ² ·2 | 0.381 | 0.988 | 24 | 39 | 0.315 | 0.911 | 20 | 39 | 1.1 | 1.2 |
| 256 ² ·2 | 0.579 | 0.989 | 42 | 39 | 0.437 | 0.933 | 28 | 39 | 1.3 | 1.5 |

Table 1: $k = 6$ BR2 discretization of the Laplace equation, three-levels p -multigrid preconditioner performance on three h -refined mesh sequences, with and without stabilization scaling. Comparison of convergence rates of the outer solver and the coarse smoother (ρ and ρ_c , respectively), comparison of the number of iterations of the outer solver and the coarse smoother (ITs and ITs $_c$, respectively), and evaluation of the speedup ($\frac{\text{wall clock time scaling off}}{\text{wall clock time scaling on}}$) considering solution CPU time and solution plus assembly CPU time (Sol and Tot, respectively).

| | Solver | | ℓ | κ_ℓ | rTol | ITs | Smoother | | | |
|---------------------|----------------------------|----------|--------------|------------------|-----------------------|----------|---------------|------------------|---------|-----|
| | FGMRES[MG ν], $L = 5$ | | 0,...,4 5 | 6 - ℓ 1 | - 10 ⁻³ | 1 400 | GMRES[ILU(0)] | | | |
| grid | scaling off | | | | scaling on | | | | speedup | |
| reg-tri | ρ | ρ_c | ITs | ITs _c | ρ | ρ_c | ITs | ITs _c | Tot | Sol |
| 39 ² ·2 | 0.0288 | 0.965 | 7 | 196 | 0.0176 | 0.885 | 6 | 57 | 1.5 | 2 |
| 79 ² ·2 | 0.0281 | 0.982 | 7 | 389 | 0.0163 | 0.913 | 6 | 76 | 1.8 | 2.5 |
| 158 ² ·2 | 0.0502 | 0.996 | 8 | 399 | 0.0186 | 0.962 | 6 | 177 | 1.8 | 2.2 |
| 311 ² ·2 | 0.102 | 0.997 | 11 | 399 | 0.0161 | 0.99 | 6 | 399 | 1.7 | 1.9 |
| dist-quad | ρ | ρ_c | ITs | ITs _c | ρ | ρ_c | ITs | ITs _c | Tot | Sol |
| 32 ² | 0.0274 | 0.908 | 7 | 72 | 0.00659 | 0.786 | 5 | 29 | 1.2 | 1.6 |
| 64 ² | 0.0267 | 0.963 | 7 | 186 | 0.0063 | 0.876 | 5 | 53 | 1.4 | 2 |
| 128 ² | 0.0215 | 0.98 | 6 | 350 | 0.00623 | 0.927 | 5 | 92 | 1.7 | 2.4 |
| 256 ² | 0.0325 | 0.995 | 7 | 399 | 0.00403 | 0.967 | 5 | 206 | 1.8 | 2.4 |
| grad-tri | ρ | ρ_c | ITs | ITs _c | ρ | ρ_c | ITs | ITs _c | Tot | Sol |
| 32 ² ·2 | 0.0684 | 0.887 | 9 | 58 | 0.0443 | 0.79 | 8 | 30 | 1.1 | 1.3 |
| 64 ² ·2 | 0.0907 | 0.957 | 10 | 157 | 0.0728 | 0.84 | 9 | 40 | 1.4 | 1.8 |
| 128 ² ·2 | 0.146 | 0.958 | 12 | 163 | 0.117 | 0.93 | 11 | 96 | 1.4 | 1.6 |
| 256 ² ·2 | 0.208 | 0.982 | 15 | 371 | 0.168 | 0.955 | 13 | 150 | 1.8 | 2.1 |
| | Solver | | ℓ | κ_ℓ | rTol | ITs | Smoother | | | |
| | FGMRES[MG ν], $L = 5$ | | 0,...,4 5 | 6 - ℓ 1 | - 10 ⁻³ | 1 40 | GMRES[ILU(0)] | | | |
| grid | scaling off | | | | scaling on | | | | speedup | |
| reg-tri | ρ | ρ_c | ITs | ITs _c | ρ | ρ_c | ITs | ITs _c | Tot | Sol |
| 39 ² ·2 | 0.166 | 0.972 | 14 | 39 | 0.0279 | 0.916 | 7 | 39 | 1.4 | 1.8 |
| 79 ² ·2 | 0.339 | 0.985 | 22 | 39 | 0.0664 | 0.94 | 9 | 39 | 1.6 | 2.2 |
| 158 ² ·2 | 0.661 | 0.991 | 55 | 39 | 0.206 | 0.983 | 15 | 39 | 2.5 | 3.3 |
| 311 ² ·2 | 0.829 | 0.988 | 122 | 39 | 0.391 | 0.979 | 25 | 39 | 3.7 | 4.6 |
| dist-quad | ρ | ρ_c | ITs | ITs _c | ρ | ρ_c | ITs | ITs _c | Tot | Sol |
| 32 ² | 0.0581 | 0.956 | 9 | 39 | 0.00658 | 0.794 | 5 | 31 | 1.2 | 1.6 |
| 64 ² | 0.139 | 0.979 | 12 | 39 | 0.00959 | 0.928 | 5 | 39 | 1.4 | 2 |
| 128 ² | 0.337 | 0.982 | 22 | 39 | 0.0442 | 0.964 | 8 | 39 | 1.7 | 2.4 |
| 256 ² | 0.613 | 0.985 | 47 | 39 | 0.137 | 0.959 | 12 | 39 | 2.5 | 3.5 |
| grad-tri | ρ | ρ_c | ITs | ITs _c | ρ | ρ_c | ITs | ITs _c | Tot | Sol |
| 32 ² ·2 | 0.0743 | 0.924 | 9 | 39 | 0.0443 | 0.82 | 8 | 35 | 1.1 | 1.1 |
| 64 ² ·2 | 0.143 | 0.975 | 12 | 39 | 0.0726 | 0.89 | 9 | 39 | 1.1 | 1.3 |
| 128 ² ·2 | 0.343 | 0.989 | 22 | 39 | 0.118 | 0.973 | 11 | 39 | 1.5 | 1.8 |
| 256 ² ·2 | 0.564 | 0.991 | 40 | 39 | 0.215 | 0.99 | 15 | 39 | 2 | 2.5 |

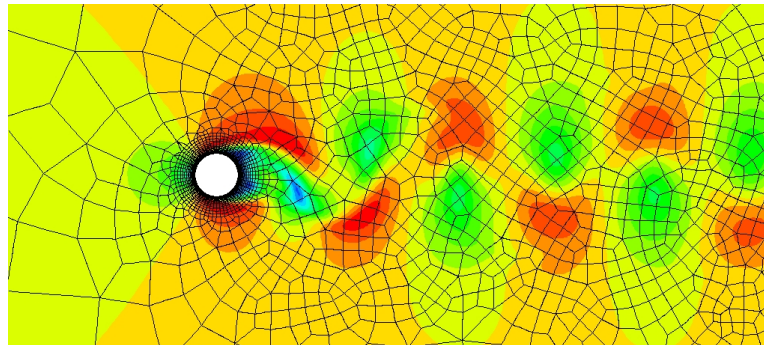
Table 2: $k = 6$ BR2 discretization of the Laplace equation, six-levels p -multigrid preconditioner performance on three h -refined mesh sequences, with and without stabilization scaling. Comparison of convergence rates of the outer solver and the coarse smoother (ρ and ρ_c , respectively), comparison of the number of iterations of the outer solver and the coarse smoother (ITs and ITs_c, respectively), and evaluation of the speedup ($\frac{\text{wall clock time scaling off}}{\text{wall clock time scaling on}}$) considering solution CPU time and solution plus assembly CPU time (Sol and Tot, respectively).

3.2. Application to the Incompressible Navier–Stokes equations

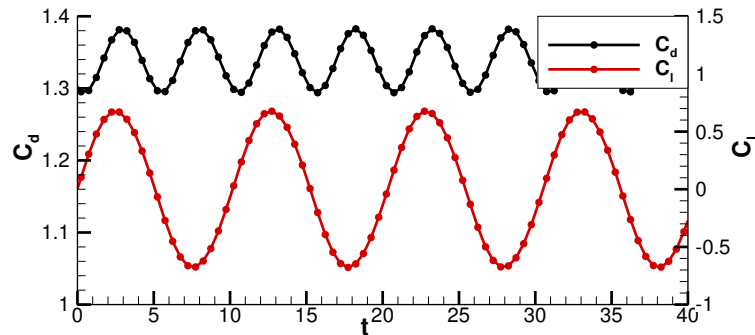
In this section the performance of the p -multigrid preconditioner, possibly coupled with the matrix-free solver, is compared to state-of-the-art single-grid strategies in the context of unsteady flow simulations. Three incompressible flow problems of increasing complexity are considered: i) the two-dimensional laminar flow around a circular cylinder at $Re = 200$; ii) the three-dimensional laminar flow around a sphere at $Re = 300$; iii) the Implicit LES of the transitional flow on a flat plate with semi-circular leading edge. This latter test case, named T3L1, is part of the ERCOFTAC (European Research Community on Flow, Turbulence and Combustion) test case suite, and is representative of the target applications for the solution strategy here proposed.

3.2.1. Laminar flow past a two-dimensional circular cylinder at $Re = 200$

The laminar flow around a circular cylinder at $Re = 200$ is solved with $k = 6$ on a computational grid made of 4710 elements with curved edges represented by cubic Lagrange polynomials. The domain extension is $[-50, 100] \times [-50, 50]$ in terms of non-dimensional units. We remark that the grid was deliberately generated with a severe grid refinement in the wake region, as well as large elements at the far-field, in order to challenge the solution strategy. Dirichlet and Neumann boundary conditions are imposed at the inflow and outflow boundaries, respectively,



(a) Velocity magnitude iso-contours



(b) C_d and C_l coefficients history

Figure 2: Laminar flow around a circular cylinder at $Re = 200$. Velocity magnitude iso-contour.

while symmetry flow conditions are employed at the top and bottom boundaries. The no-slip Dirichlet boundary condition is imposed on the cylinder wall. A snapshot of the mesh and the velocity magnitude contours is shown in Fig. 2(a). Time marching is performed by means of the linearly-implicit four-stage, order three ROSI2PW Runge-Kutta method [25]. The scheme is specifically designed to accurately deal with PDAEs of index 2, like the INS equations. A non-dimensional fixed time step $\Delta t = 0.25$, corresponding to 1/20 of the shedding period, is found to be adequate to describe the flow physics and large enough to stress the solution strategy. Fig. 2(b) reports lift and drag coefficients history. The drag coefficient $C_d = 1.335$ and the Strouhal number $St = 0.1959$ are in good agreement with [37] and references therein. Even if, for the sake of efficiency, it is possible to adaptively estimate the relative defect drop rTol that the linear solver should attain [10], we set the fix value $rTol = 10^{-5}$ to compare different preconditioners with the same forcing term. The resulting time discretization error, estimated using the embedded Runge-Kutta scheme, is small enough not to affect the overall solution accuracy. Moreover, the defect tolerance is large enough to ensure that the matrix-free approximation error does not affect GMRES convergence, see [10]. The right preconditioning approach is employed throughout all the numerical experiments of this paper to reach convergence levels independent of the preconditioner.

Performance assessment. The p -multigrid preconditioner approach seeks to minimize the number of GMRES iterations on the fine grid by means of a full p -multigrid solution strategy. A full \mathcal{V} -cycle p -multigrid iteration (see Algorithm 3) has many parameters to tune in order to get the best performance, among the others we mention the following: i) the choice of the smoother and its preconditioner on each level, ii) the number of smoothing iteration on each level, iii) the forcing term (controlling the exit condition based on the relative defect drop) of the coarse solver and its maximum number of iterations. Accordingly the combination of these parameters lead to a multitude of different configurations that is hard to explore comprehensively. Nevertheless, we provide some useful indications that can be directly applied to the simulation of realistic flow problems. In general, with respect to the test cases proposed in Section 3.1, the use of a full p -multigrid strategy together with an increased number of smoothing iterations proved to deal more efficiently with the non-linearity of the governing equations. The experiments are devoted to show the benefits of i) using a rescaled-inherited approach for the coarse space operators to improve the convergence rates of the iterative solver; ii) apply a matrix-free approximation to the fine space to reduce the memory footprint and increase the computational efficiency. Code profiling is applied for 10 time steps starting from a fully developed flow solution obtained with the same polynomial degree, same time step size and solving linear system up to the same tolerance. In practice, the performance of the preconditioners is evaluated on the solution of 40 linear systems. The efficiency of each setting is monitored in parallel, to assess the behavior of different preconditioners in a realistic setup for this kind of computations. The runs are performed on a computational node made by two sixteen-core AMD Opteron CPUs. First, we report in Table 3 the results obtained using single-grid preconditioners. As expected, the numerical experiments show a sub-optimal parallel efficiency for the BJ preconditioner, indeed the average number of linear iterations increases while increasing the number of sub-domains. The iterations number increase tops at 62% when comparing the simulation on 16 cores against the serial one. The ASM(1,ILU(0)) preconditioner partially heals the performance degradation providing a 10% increase of the iterations number at the expenses of a higher memory requirement, as explained in Section 2.5. The matrix-based and the matrix-free versions of GMRES provide a similar number of iterations with a CPU time that is in favour of the former. This can be explained by the high

quadrature cost associated to non-affine mesh elements, see *e.g.*[38]. In fact, while Franciolini *et al.*[10] demonstrated that the residual computation and a matrix-vector product has similar costs when dealing with high-order discretizations on affine elements, in this case the numerical quadrature expense has a higher relative cost on residual evaluation. It is worth pointing out that no attempt was made to optimize numerical quadrature, in particular elements located far from curved boundaries are still treated as high-order non-affine elements for the sake of simplicity. Even if matrix-free iterations can be further improved in term of efficiency in realistic applications, this is beyond the scope of the present work. Table 4 allows to evaluate the impact of the fine smoother preconditioner on the computational efficiency. We report two parameters of interest, the average number of FGMRES iterations (ITs) and the speed-up with respect to the best

| Solver Prec | GMRES(MB) | | GMRES(MB) | | GMRES(MF) | | GMRES(MF) | | GMRES(MF) | |
|----------------|-----------|---------|---------------|---------|-----------|---------|-----------|---------|---------------|---------|
| | BJ | | ASM(1,ILU(0)) | | EWBJ | | BJ | | ASM(1,ILU(0)) | |
| nProcs | ITs | TotTime | ITs | TotTime | ITs | TotTime | ITs | TotTime | ITs | TotTime |
| 1 | 123.5 | 3805 | 123.5 | 3805 | 542.8 | 36700 | 112.2 | 9860 | 112.2 | 9860 |
| 2 | 108.0 | 1756 | 121.3 | 1917 | 538.7 | 17980 | 102.4 | 4547 | 109.9 | 4782 |
| 4 | 105.3 | 859 | 123.9 | 982 | 543.9 | 9281 | 103.5 | 2325 | 111.2 | 2426 |
| 8 | 138.0 | 543 | 120.4 | 515 | 542.2 | 4615 | 121.4 | 1333 | 111.2 | 1253 |
| 16 | 199.7 | 497 | 134.7 | 378 | 554.4 | 2934 | 171.3 | 995 | 122.8 | 750 |

Table 3: Two-dimensional cylinder test case. Single-grid parallel performances, matrix-based and matrix-free implementations. Comparison of the average number of GMRES iterations (ITs) and the whole elapsed CPU time (solution plus assembly) TotTime.

| Solver | ℓ | κ_ℓ | Tol | ITs | Smoother | Prec | | |
|-----------------------------|-----------|------------------|----------------------|------------------|-----------|------------------|-------------|------------------|
| FGMRES[MG _{full}] | 0,1 | 6,2 | – | * | GMRES(MB) | ‡ | | |
| | 2 | 1 | – | 40 | GMRES(MB) | ASM(1,ILU(0)) | | |
| scaling off | *3 ‡BJ | | *3 ‡ASM(1,ILU(0)) | | *8 ‡BJ | | *8 ‡EWBJ | |
| nProcs | ITs | SU _{MB} | ITs | SU _{MB} | ITs | SU _{MB} | ITs | SU _{MB} |
| 1 | 4.10 | 2.02 | 4.10 | 1.98 | 2.98 | 1.76 | 5.48 | 1.56 |
| 2 | 4.63 | 1.82 | 4.05 | 1.90 | 3.10 | 1.65 | 5.48 | 1.49 |
| 4 | 5.73 | 1.65 | 4.05 | 1.90 | 3.63 | 1.53 | 5.63 | 1.48 |
| 8 | 7.20 | 1.39 | 4.35 | 1.74 | 3.85 | 1.40 | 5.63 | 1.40 |
| 16 | 8.63 | 1.37 | 5.38 | 1.71 | 5.05 | 1.28 | 5.70 | 1.53 |
| scaling on | 3* ‡BJ | | *3 ‡ASM(1,ILU(0)) | | *8 ‡BJ | | *8 ‡EWBJ | |
| nProcs | ITs | SU _{MB} | ITs | SU _{MB} | ITs | SU _{MB} | ITs | SU _{MB} |
| 1 | 3.43 | 2.11 | 3.43 | 2.11 | 2.48 | 1.88 | 3.50 | 1.92 |
| 2 | 3.68 | 1.99 | 3.55 | 1.97 | 2.80 | 1.72 | 3.53 | 1.84 |
| 4 | 4.78 | 1.79 | 3.60 | 1.95 | 2.55 | 1.80 | 3.83 | 1.79 |
| 8 | 5.13 | 1.51 | 3.60 | 1.74 | 2.58 | 1.57 | 3.68 | 1.60 |
| 16 | 7.65 | 1.20 | 4.10 | 1.67 | 2.85 | 1.49 | 3.50 | 1.68 |

Table 4: Two-dimensional cylinder test case. Effects of the smoother type and the rescaled-inherited coarse spaces on parallel performance. Comparison of the average number of FGMRES iterations (ITs) and the speed-up (SU_{MB}) of the p -multigrid preconditioner with respect to the best performing single-grid preconditioner. The asterisk and the double dagger symbols in the solver specs row are placeholders for the number of iterations (ITs) and coarse solver type of each column, respectively.

performing single-grid preconditioner, $SU_{MB} = \text{TotTime}/\text{TotTime}_{\text{ref}}$, where $\text{TotTime}_{\text{ref}}$ is the total CPU time of the GMRES(MB)[ASM(1,ILU(0))] approach. The specs of the p -multigrid iteration setup are reported in the top of the table. We also compare the standard-inherited approach (*scaling off*) with the rescaled-inherited one (*scaling on*).

FGMRES[MG_{full}] with 3 GMRES(MB)[BJ] smoothing iterations provides a speed-up of about 2 in serial computations with respect to the reference strategy. Although the solver is still faster than the reference one, the parallel performance is not satisfactory being an increase in the number of iterations observed. As expected a better scalability can be obtained with 3 GMRES(MB)[ASM(1,ILU(0))] smoothing iterations. The numerical experiment revealed that to increase the number of iterations from 3 to 8 is mandatory to maintain the smoothing efficiency of GMRES(MB)[EWBJ], and to achieve a satisfactory performance in parallel. Indeed, despite being less performing in serial runs, the number of iterations is almost independent from the number of processes. It is worth noting that increasing the number of iterations of GMRES(MB)[BJ] does not pay off in terms of speedup. The number of FGMRES iterations is significantly reduced in all the cases when considering rescaled-inherited coarse grid operators. Although the strategy does not always pay off in terms of speedup because of the increased expense of building coarse grid operators, the GMRES(MB)[EWBJ] smoother applied to rescaled-inherited coarse operator is competitive with more expensive preconditioners in parallel computations. Interestingly, the EWBJ preconditioner is the cheapest from the memory footprint viewpoint.

Table 5 compares the computational efficiency when varying the preconditioner on the coarsest level. The cheapest and efficient GMRES(MB)[EWBJ] smoother is employed on all levels but the coarsest. The top and bottom of the table include results for a matrix-based and a matrix-free approach, respectively. Note that only on the finest level matrix-vector products are performed matrix free, both within the outer FGMRES iteration and the fine GMRES smoother. Indeed, since the coarse levels operators are fairly inexpensive to store in memory, the moderate memory savings of a matrix-free implementation would not justify the increased computational costs. The results highlight that a further improvement in computational efficiency is achieved by means of a [ASM(1,ILU(1))] preconditioner for the coarsest smoother: the number of FGMRES iterations decreases while maintain optimal scalability and the speedup values for the matrix-free approach increase when considering more sub-domains. Due to low polynomial degree of the coarsest level, the additional level of fill of the ILU factorization is not significant from the memory footprint viewpoint. Interestingly, the increased robustness of the rescaled-inherited p -multigrid approach results in similar speedups for all the coarse level solver options. For the matrix-free implementation we report two different speedup values i) SU_{MB} considers as a reference the GMRES(MB)[ASM(1,ILU(0))] solver, that is the best performing matrix-based single-grid strategy, ii) SU_{MF} considers as a reference the GMRES(MF)[BJ] solver, that is the best performing matrix free single-grid strategy. We disregard the inefficient GMRES(MF)[EWBJ] configuration despite being the less demanding solver from the memory viewpoint. Since the relative cost of the solution with respect to matrix assembly is higher in a matrix-free implementation, reducing the number of FGMRES iterations does pay off. Accordingly the benefits of rescaled-inherited coarse grid operator are more evident: the total execution time is comparable with GMRES(MB)[ASM(1,ILU(0))] and almost three times faster than GMRES(MF)[BJ].

To conclude Table 6 compares three- and four-levels p -multigrid preconditioners. The additional level significantly reduces the number of FGMRES iterations at the expense of storing a fourth degree coarse grid operator. Once again the benefits in terms of speedup are most significant in the matrix-free framework, where solution times dominates assembly times. Matrix-free rescaled-inherited p -multigrid is 30% faster then the best performing matrix-based single-grid

solver and 3.5 times faster than the best performing matrix-free single-grid solver.

| Solver | ℓ | κ_ℓ | Tol | ITs | Smoother | Prec |
|-----------------------------|-------------------|------------------|------------------------------|------------------|------------------------------|------------------|
| FGMRES[MG _{full}] | 0 | 6 | – | 8 | * | EWBJ |
| | 1 | 2 | – | 8 | GMRES(MB) | EWBJ |
| | 2 | 1 | – | 40 | GMRES(MB) | ‡ |
| scaling off | *GMRES(MB) ‡BJ | | *GMRES(MB) ‡ASM(1,ILU(0)) | | *GMRES(MB) ‡ASM(1,ILU(1)) | |
| nProcs | ITs | SU _{MB} | ITs | SU _{MB} | ITs | SU _{MB} |
| 1 | 5.48 | 1.56 | 5.48 | 1.56 | 4.73 | 1.64 |
| 2 | 5.63 | 1.47 | 5.48 | 1.49 | 4.73 | 1.56 |
| 4 | 5.43 | 1.52 | 5.63 | 1.48 | 4.73 | 1.57 |
| 8 | 5.90 | 1.38 | 5.63 | 1.40 | 4.75 | 1.47 |
| 16 | 6.85 | 1.37 | 5.70 | 1.53 | 4.95 | 1.62 |
| scaling on | *GMRES(MB) ‡BJ | | *GMRES(MB) ‡ASM(1,ILU(0)) | | *GMRES(MB) ‡ASM(1,ILU(1)) | |
| nProcs | ITs | SU _{MB} | ITs | SU _{MB} | ITs | SU _{MB} |
| 1 | 3.50 | 1.92 | 3.50 | 1.92 | 3.15 | 1.96 |
| 2 | 3.55 | 1.85 | 3.53 | 1.84 | 3.15 | 1.88 |
| 4 | 3.35 | 1.91 | 3.83 | 1.79 | 3.15 | 1.89 |
| 8 | 3.33 | 1.70 | 3.68 | 1.60 | 3.15 | 1.67 |
| 16 | 3.48 | 1.70 | 3.50 | 1.68 | 3.18 | 1.73 |
| scaling off | *GMRES(MF) ‡BJ | | *GMRES(MF) ‡ASM(1,ILU(0)) | | *GMRES(MF) ‡ASM(1,ILU(1)) | |
| nProcs | SU _{MB} | SU _{MF} | SU _{MB} | SU _{MF} | SU _{MB} | SU _{MF} |
| 1 | 0.61 | 1.59 | 0.61 | 1.59 | 0.69 | 1.80 |
| 2 | 0.60 | 1.41 | 0.61 | 1.45 | 0.69 | 1.63 |
| 4 | 0.60 | 1.42 | 0.59 | 1.41 | 0.69 | 1.63 |
| 8 | 0.55 | 1.43 | 0.57 | 1.48 | 0.66 | 1.70 |
| 16 | 0.61 | 1.61 | 0.73 | 1.92 | 0.77 | 2.03 |
| scaling on | *GMRES(MF) ‡BJ | | *GMRES(MF) ‡ASM(1,ILU(0)) | | *GMRES(MF) ‡ASM(1,ILU(1)) | |
| nProcs | SU _{MB} | SU _{MF} | SU _{MB} | SU _{MF} | SU _{MB} | SU _{MF} |
| 1 | 0.89 | 2.31 | 0.89 | 2.30 | 0.98 | 2.54 |
| 2 | 0.92 | 2.18 | 0.89 | 2.11 | 0.98 | 2.32 |
| 4 | 0.93 | 2.21 | 0.87 | 2.06 | 0.97 | 2.30 |
| 8 | 0.86 | 2.23 | 0.85 | 2.20 | 0.92 | 2.39 |
| 16 | 1.06 | 2.80 | 1.07 | 2.81 | 1.16 | 3.05 |

Table 5: Two-dimensional cylinder test case. Effects of the coarse level solver on parallel performance. Comparison of the average number of FGMRES iterations (ITs) and the speed-up of the p -multigrid preconditioner with respect to the best performing single-grid preconditioner in its matrix-based and matrix-free implementation (SU_{MB} and SU_{MF}, respectively). The asterisk and the double dagger symbols in the solver specs row are placeholders for the smoother and coarse solver types of each column, respectively.

3.2.2. Three-dimensional laminar flow past a sphere at $Re = 300$

As a three-dimensional validation test case we computed the unsteady laminar flow past a sphere at $Re = 300$ [39, 40, 41, 42]. The solution is characterised by a perfectly periodic behaviour, with the flow maintaining a plane of symmetry. In our computations, the symmetry plane was enforced by defining a proper boundary condition. The mesh is made of 3560 elements with a bi-quadratic geometrical representation of the wall boundary, see Fig. 3(a). The computational domain is obtained via extrusion of the wall surface discretization. While the no-slip condition is set at the wall, velocity inflow and pressure outflow boundary conditions are imposed on the spherical farfield located at 50 diameters. A $k = 6$ representation of the solution was employed for all computations presented hereafter. We remark that the small number of mesh elements together with the lack of a refined region in the wake of the sphere reduce the stiffness of the problem. The parallel performance is evaluated running on the Marconi-A1 HPC platform hosted by CINECA, the italian supercomputing center. Scalability is assessed on a single-node base, as the CPU time of the serial computation exceeded the maximum wall-clock time allowed by CINECA. The number of mesh elements is optimised to ensure that all the solution strategies fit the memory of a single node (118 GB). Despite the small size of the problem the following numerical experiments aim at providing reliable indications on the parallel performance that can be extended to real-size production runs.

The solution is accurately integrated in time with a fixed non-dimensional time step $\delta t = 0.5$ and a relative tolerance on the linear system defect drop of $rTol = 10^{-5}$. The drag coefficient time history is shown in Fig. 3(b), its mean value reads 0.659, and the Strouhal number is $St = 0.133$, in agreement with the published literature, see [42]. Despite the geometry being represented

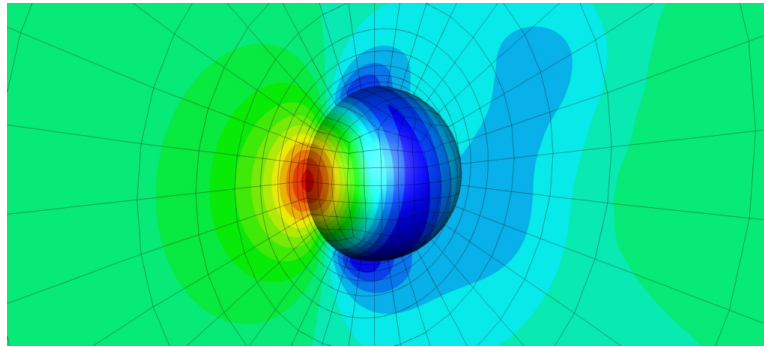
| Solver | ℓ | κ_ℓ | rTol | ITs | Smoother | Prec | | |
|-----------------------------|------------------------------------|--------------------------------------|------------------------------------|--------------------------------------|------------------|------------------|------------------|------------------|
| | 0 | 6 | - | 8 | * | EWBJ | | |
| FGMRES[MG _{full}] | 1,...,L-1 | ‡ | - | 8 | GMRES(MB) | EWBJ | | |
| | L | 1 | - | 40 | GMRES(MB) | ASM(1,ILU(1)) | | |
| scaling off | GMRES(MB)* 2^{\ddagger} (L=2) | GMRES(MB)* $4,2^{\ddagger}$ (L=3) | GMRES(MF)* 2^{\ddagger} (L=2) | GMRES(MF)* $4,2^{\ddagger}$ (L=3) | | | | |
| nProcs | ITs | SU _{MB} | ITs | SU _{MB} | SU _{MB} | SU _{MF} | SU _{MB} | SU _{MF} |
| 1 | 4.73 | 1.64 | 3.00 | 1.62 | 0.69 | 1.80 | 0.88 | 2.29 |
| 2 | 4.73 | 1.56 | 3.00 | 1.53 | 0.69 | 1.63 | 0.87 | 2.06 |
| 4 | 4.73 | 1.57 | 3.00 | 1.54 | 0.69 | 1.63 | 0.87 | 2.05 |
| 8 | 4.75 | 1.47 | 3.10 | 1.43 | 0.66 | 1.70 | 0.78 | 2.02 |
| 16 | 4.95 | 1.62 | 3.33 | 1.55 | 0.77 | 2.03 | 0.97 | 2.54 |
| scaling on | GMRES(MB)* 2^{\ddagger} (L=2) | GMRES(MB)* $4,2^{\ddagger}$ (L=3) | GMRES(MF)* 2^{\ddagger} (L=2) | GMRES(MF)* $4,2^{\ddagger}$ (L=3) | | | | |
| nProcs | ITs | SU _{MB} | ITs | SU _{MB} | SU _{MB} | SU _{MF} | SU _{MB} | SU _{MF} |
| 1 | 3.15 | 1.96 | 2.00 | 1.91 | 0.98 | 2.54 | 1.19 | 3.09 |
| 2 | 3.15 | 1.88 | 2.00 | 1.82 | 0.98 | 2.32 | 1.18 | 2.80 |
| 4 | 3.15 | 1.89 | 2.00 | 1.83 | 0.97 | 2.30 | 1.19 | 2.82 |
| 8 | 3.15 | 1.67 | 2.00 | 1.63 | 0.92 | 2.39 | 1.11 | 2.87 |
| 16 | 3.18 | 1.73 | 2.00 | 1.72 | 1.16 | 3.05 | 1.33 | 3.50 |

Table 6: Two-dimensional cylinder test case. Comparison of a three-level and four-level p -multigrid strategy in optimal settings for matrix-based and matrix-free fine level options.

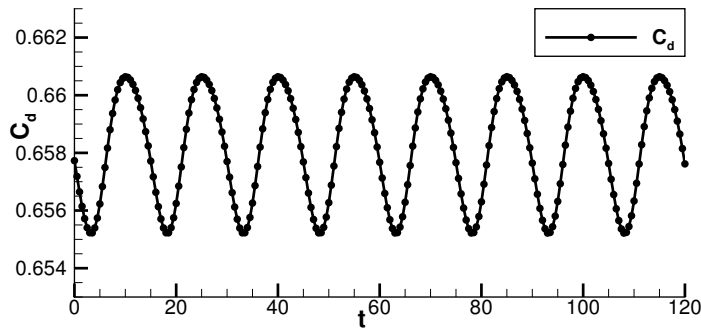
with second degree polynomial spaces, the degree of exactness of quadrature rules does not consider the degree of mappings from reference to physical mesh elements. Accordingly bilinear forms are exactly integrated only over affine mesh elements, located far away from the sphere boundaries. We numerically verified that, for this test case, this practice does not compromise accuracy while significantly improving the matrix-free computational time, see [10]. For the sake of efficiency of parallel runs, the mesh has been partitioned using the *local* two-level partitioning strategy described in [43]. The first-level decomposition is performed according to the number of nodes, thus, the second-level decomposition further decompose each node-local partition according to the number of cores per node, such that the extra-node MPI communications are minimized.

Performance assessment. Table 7 reports the parallel performance of the single-grid matrix-based and matrix-free solvers running in parallel up to 576 cores (6 elements per partition on average). Increasing the number of sub-domains from 36 to 576 leads to an increased number of GMRES iterations: 42% and 20% up when employing a BJ and an ASM(1,ILU(0)) preconditioner, respectively. Thanks to the use of quadrature rules suited for affine meshes, the CPU time of the matrix-free solver is similar to the matrix-based one.

Results reported in Table 8 for a three- and four-levels p -multigrid strategy and the exact



(a) C_p iso-contours



(b) C_D

Figure 3: Laminar flow around a Sphere at $Re = 300$. Pressure coefficient iso-contours (top) and drag coefficient history (bottom).

same setup of two-dimensional computations confirm the efficacy of the multigrid preconditioner: the number of iterations stays the same up to 576 cores and the speedup are maintained in this largely-parallelized scenario. Stabilization scaling provides slight improvements in terms of FGMRES iterations and computation time, despite the small number of mesh elements. The four-level p -multigrid preconditioner is almost two times faster than the best single-grid setup.

| Solver Prec | GMRES(MB) | | GMRES(MB) | | GMRES(MF) | | GMRES(MF) | |
|----------------|-----------|---------|---------------|---------|-----------|---------|---------------|---------|
| | BJ | | ASM(1,ILU(0)) | | BJ | | ASM(1,ILU(0)) | |
| nProcs | ITs | TotTime | ITs | TotTime | ITs | TotTime | ITs | TotTime |
| 36 | 78.5 | 1448.1 | 34.5 | 1245.9 | 77.1 | 1365.9 | 34.7 | 1220.7 |
| 72 | 86.7 | 774.0 | 35.0 | 675.2 | 87.0 | 743.9 | 35.0 | 671.9 |
| 144 | 84.9 | 380.1 | 38.2 | 386.7 | 85.2 | 370.3 | 38.2 | 381.9 |
| 288 | 102.7 | 226.7 | 40.2 | 233.1 | 102.4 | 221.3 | 40.3 | 228.5 |
| 576 | 111.8 | 126.0 | 41.3 | 150.6 | 113.6 | 129.2 | 41.3 | 133.8 |

Table 7: Three dimensional incompressible flow around a sphere. Single-grid parallel performances, matrix-based and matrix-free implementations. Comparison of the average number of GMRES iterations (ITs) and the whole elapsed CPU time (solution plus assembly) TotTime. Computations performed on Marconi-A1@CINECA.

| Solver | ℓ | κ_ℓ | rTol | ITs | Smoother | Prec | | |
|-----------------------------|------------------------|------------------|--------------------------|------------------|------------------------|------------------|--------------------------|------------------|
| | 0 | 6 | - | 8 | * | EWBJ | | |
| FGMRES[MG _{full}] | 1,...,L-1 | ‡ | - | 8 | GMRES(MB) | EWBJ | | |
| | L | 1 | - | 40 | GMRES(MB) | ASM(1,ILU(0)) | | |
| scaling off | *GMRES(MB) ‡2 (L=2) | | *GMRES(MB) ‡4,2 (L=3) | | *GMRES(MF) ‡2 (L=2) | | *GMRES(MF) ‡4,2 (L=3) | |
| nProcs | ITs | SU _{MB} | ITs | SU _{MB} | SU _{MB} | SU _{MF} | SU _{MB} | SU _{MF} |
| 36 | 4.00 | 1.29 | 2.00 | 1.61 | 1.37 | 1.29 | 2.28 | 2.15 |
| 72 | 4.00 | 1.37 | 2.00 | 1.68 | 1.52 | 1.46 | 2.38 | 2.29 |
| 144 | 4.00 | 1.29 | 2.00 | 1.43 | 1.45 | 1.41 | 2.07 | 2.02 |
| 288 | 4.00 | 1.37 | 2.00 | 1.67 | 1.56 | 1.52 | 2.14 | 2.09 |
| 576 | 4.00 | 1.28 | 2.00 | 1.55 | 1.46 | 1.50 | 1.55 | 1.59 |
| scaling on | GMRES(MB)* ‡2 (L=2) | | *GMRES(MB) ‡4,2 (L=3) | | *GMRES(MF) ‡2 (L=2) | | *GMRES(MF) ‡4,2 (L=3) | |
| nProcs | ITs | SU _{MB} | ITs | SU _{MB} | SU _{MB} | SU _{MF} | SU _{MB} | SU _{MF} |
| 36 | 3.0 | 1.43 | 2.00 | 1.51 | 1.53 | 1.44 | 2.09 | 1.97 |
| 72 | 3.0 | 1.52 | 2.00 | 1.61 | 1.62 | 1.56 | 2.18 | 2.09 |
| 144 | 3.0 | 1.36 | 2.00 | 1.50 | 1.55 | 1.51 | 1.93 | 1.88 |
| 288 | 3.0 | 1.56 | 2.00 | 1.60 | 1.71 | 1.67 | 2.02 | 1.97 |
| 576 | 3.0 | 1.45 | 2.00 | 1.43 | 1.63 | 1.67 | 1.73 | 1.78 |

Table 8: Three dimensional incompressible flow around a Sphere. Efficiency of a three and four level p -multigrid strategy varying the fine level smoother. Comparison of the average number of FGMRES iterations (ITs) and the speed-up of the p -multigrid preconditioner with respect to the best performing single-grid preconditioner in its matrix-based and matrix-free implementation (SU_{MB} and SU_{MF}, respectively). The asterisk and the double dagger symbols in the solver specs row are placeholders for the smoother and coarse solver types of each column, respectively. Computations performed on Marconi-A1@CINECA.

3.3. Application to the under-resolved simulation of turbulent flows

In this section the devised matrix-free implementation coupled with the rescaled-inherited p -multigrid preconditioner is applied to the implicit LES of the transitional flow on a flat plate with a semi-circular leading edge of diameter d at $Re_d = 3450$ and a low level of free-stream turbulence intensity ($Tu = 0.2\%$). This test case, named T3L1, is part of the ERCOFTAC test case suite. The solution exhibits at leading edge a laminar separation bubble and, downstream the transition, an attached turbulent boundary layer. Those complex flow features are perfectly suited to evaluate the efficiency of the solver and highlight the advantages of using a dG-based ILES approach. ILES naturally resolves all the flow scales (in a DNS-fashion) if the numerical resolution is enough to do so, while the numerical dissipation plays the role of a sub-grid scale model for the spatially under-resolved regions of the domain. In this test case, the laminar region is fully resolved, while in the turbulent region the dissipation of the numerical scheme dumps the under-resolved scales.

The simulations were performed in parallel using 540 cores on a hybrid mesh of 38320 elements with curved edges. The unstructured grid is strongly coarsened moving away from the plate, while a structured-like boundary layer is used at the wall. The first cell height is $10^{-2}d$ and the mesh is refined near the reattachment region, where the minimum dimension along x axis is $2 \cdot 10^{-2}d$, see Fig. 4. The domain extension on the $x - y$ plane is taken from [44], *i.e.*, $28d \times 17d$, and it is extruded using 10 elements along the span-wise direction z for a length of $2d$, as in [45]. To our best knowledge, only those two works report a LES simulation of this ERCOFTAC test case. In both the cases, the numerical method was based on a standard second-order scheme and a dynamic subgrid scale model. A direct comparison of the present computations with previously published works in terms of DoFs is not trivial due to the differences of the computational domains. In [45] the DoFs count per variable is on the order of $1.88 \cdot 10^6$ and the domain extension in the $x - y$ plane is 1.9 times smaller. In [44] the Dofs count is on the order of $4.39 \cdot 10^6$ and the domain is 4 times larger in the span-wise direction. The result with the lowest resolution presented in this paper has about $1.39 \cdot 10^6$ DOFs and takes advantage of the unstructured nature of the grid by increasing the mesh density along the turbulent wake, that is for $x/d \gtrsim 4.5$ up to the outflow.

Physical discussion. This type of flow problem is reported to be very sensitive to the free-stream turbulence at the inlet (Tu). The free-stream flow was carefully manipulated to reproduce those

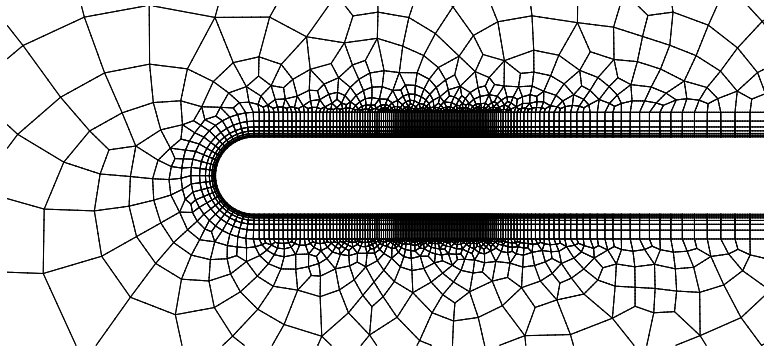


Figure 4: T3L1 test case. Near-wall detail of the computational grid.

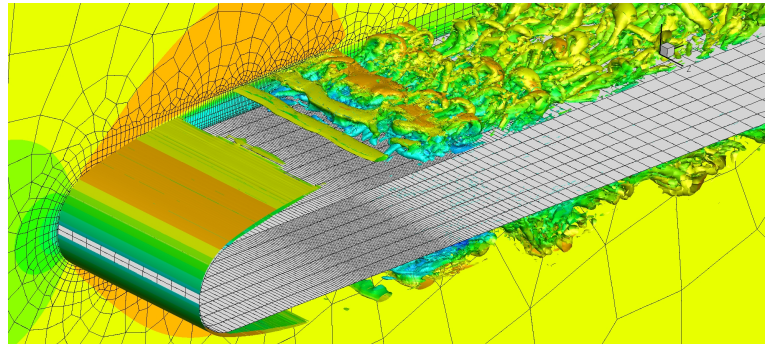
reported by ERCOFTAC as well as previous numerical computations [45, 44]. In those works, a white-noise random perturbation was added at the inflow velocity to mimic the low experimental turbulence level, *i.e.*, $Tu < 0.2\%$. In the present work, due to an aggressive mesh coarsening in the far-field regions, the generation of a free-stream turbulence at inlet is unfeasible. In fact, the coarse spatial discretization at far-field would rapidly damp any random perturbation introduced upstream. Accordingly, the turbulent fluctuations were synthetically injected, via a spatially-supported random forcing term, in those regions of the domain where the mesh density is enough not to dissipate small scales. The random forcing analytic expression assumes a Gaussian distribution in the x direction and is homogeneous in $y-z$

$$f_i = Ae^{\left(-\frac{x_1-\bar{x}_1}{2\mu}\right)}r_i \quad (33)$$

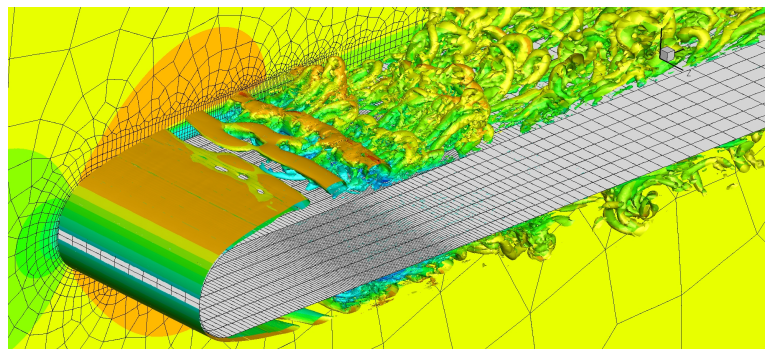
where A , \bar{x}_1 , μ and r_i are, respectively, the amplitude coefficient, the location of the forcing plane, the amplitude of the Gaussian support and a normalised random vector component such that $\sqrt{r_i r_i} = 1$. The Gaussian function was centered in $\bar{x}_1/D = -3$, and the constants A , μ were adjusted, via trial and error approach, to meet the experimental Tu levels. We avoid a fine control algorithm of the turbulent length-scale since the reattachment length is pretty insensitive to this value, see [46, 47, 48]. In the present configuration the expected turbulence intensity is met setting $A = 0.06$ and $\mu = 0.01$. We remark that perturbing the velocity field through a forcing term in the momentum equations guarantees a divergence-free perturbation.

Fig. 5 depicts the instantaneous flow fields computed with $Tu = 0\%$ and $Tu = 0.2\%$. In both cases, the quasi two-dimensional Kelvin-Helmholtz instabilities in the shear-layer region above the separation bubble and their convection downstream are observed. As expected, the low free-stream turbulence intensity value promotes the instability of the quasi two-dimensional structures arising from the upstream flow separation. For both the conditions, hairpin vortices developing after flow reattachment and the breakdown to turbulence are similar. Distortion along the spanwise direction is anticipated upstream in the $Tu = 0.2\%$ case.

As reported in previous studies, the bubble length is found to be very sensitive to the inlet turbulence intensity, see for example [49]. In particular, when increasing the Tu from 0% to 0.2% the bubble length reduces from $x_R/d = 3.90$ to 2.69 , as shown by the statistically-converged time and spanwise averaged velocity contours in Figs. 6 and 7. The length predicted for the $Tu = 0.2$ case is in a better agreement with the experimental data ($l/d = 2.75$) than other numerical computations [45, 44] (2.59 and 3.00 , respectively). Moreover, we verified by lowering the polynomial degree of the dG discretization that our statistical average x_R/d is almost converged with respect to the spatial resolution: for $k = 5$ and $k = 4$ we obtain 2.70 and 2.73 , respectively. Convergence of the statistics is also confirmed by polynomial degree independence observed for the skin friction coefficients, see Fig. 8. As opposite to the behavior documented in [45], no hysteresis effects are observed in our computations. Accordingly, if the random source term generating small turbulent perturbations is suddenly suppressed in the fully developed flow field at $Tu = 0.2\%$, the solution of a zero free-stream turbulence case is quickly recovered. Figure 9 compares velocity profiles with the experimental ones. We consider the mean stream-wise velocity $\langle u \rangle$, and the velocity fluctuation (or velocity RMS), $\langle u'u' \rangle$, as a function of the normal direction for different stations. Velocity is normalized by the local maximum velocity u_{max} , computed independently for each of the stations. The random forcing efficacy is demonstrated by the very good agreement with experimental data close to the plate stagnation point. We point out that for $x_1/l < 1.64$ improvements with respect to previous computational investigations are difficult to evaluate. As opposite, for $x_1/l > 1.64$ our results still compare favourably with the experimental data, while



(a) $Tu = 0\%$



(b) $Tu = 0.2\%$

Figure 5: T3L1 test case, $k = 6$ solutions for different Tu levels. $\lambda_2 = -1$ iso-contour and periodic plane coloured by the streamwise velocity.

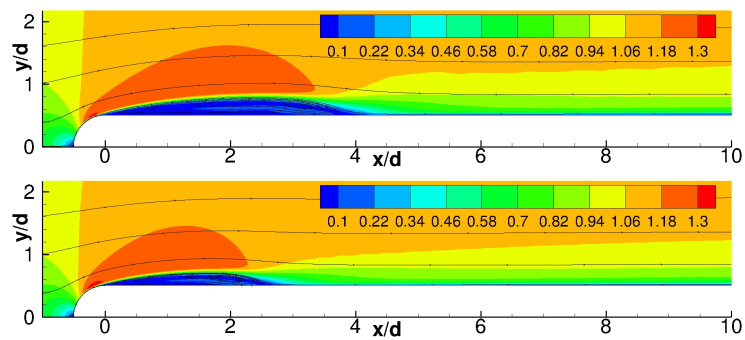


Figure 6: T3L1 test case. Effect of the Tu level. Average velocity magnitude iso-contours, $k = 6$ solutions. Top: $Tu = 0.0\%$; Bottom: $Tu = 0.2\%$.

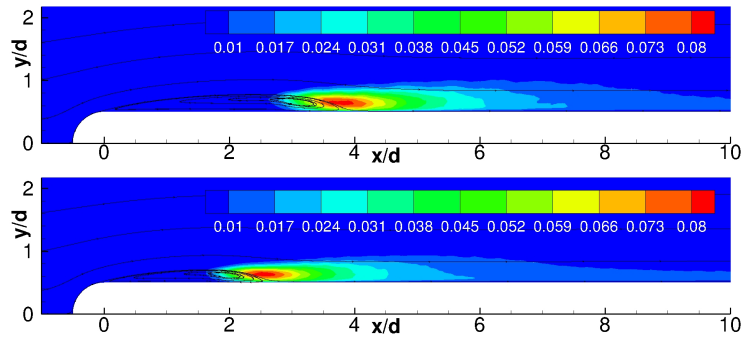


Figure 7: T3L1 test case. Effect of the Tu level. Turbulent kinetic energy iso-contours, $k = 6$ solutions. Top: $Tu = 0.0\%$; Bottom: $Tu = 0.2\%$.

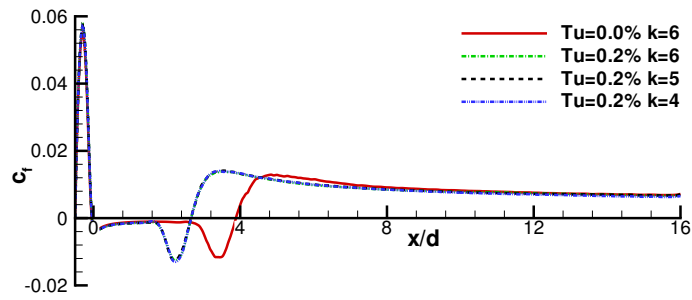


Figure 8: T3L1 test case. Effect of the Tu level on the skin friction coefficient c_f .

the matching is less evident in [44]. We stress that our velocity fluctuations compare favourably with the experiments up to $3.45l$, which was omitted in previous works, see Figures 9 and 10. This supports the claim that present computations provide a larger fully resolved region, all the polynomial degrees here considered. Note that some jumps at inter-element boundaries are still noticeable, especially for $k = 4$. Fig. 11 reports the computed averaged velocity profiles in wall units, for different stations located downstream to the reattachment region. For $x/l \geq 3.45$ the profile approaches the turbulent law of the wall, showing some discrepancies with respect to the equilibrium boundary layer in the outer layer. For the sake of comparison, the zero pressure gradient flat plate DNS result at $Re_\theta = 300$ of Spalart [50] is reported together with the numerical solution at $x/l = 4.55$, which shows almost the same Re_θ . We remark that the station at $x/l = 3.45$ is compared to the experimental data, $Re_\theta \approx 270$.

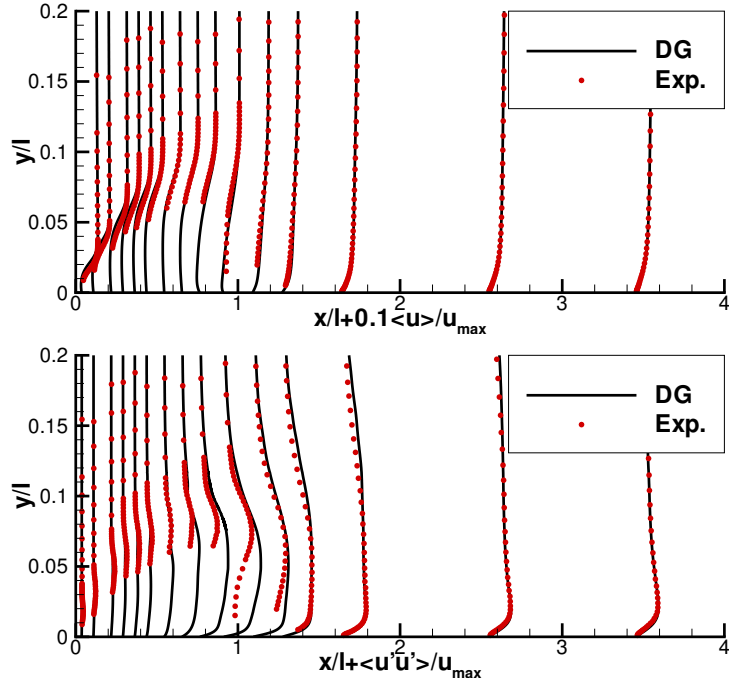


Figure 9: T3L1 test case, $k = 6$ solution for $Tu = 0.2\%$. Time- and spanwise-averaged velocity profiles in comparison with experimental data [51]. Mean (top) and RMS (bottom) flow velocity. Abscissas are non-dimensionalized using the experimental reattachment length $l/d = 2.75$.

Performance assessment. Table 9 reports the computational performances of the different solution strategies obtained for a dG approximation with $k = 6$, the same polynomial degree of reference employed in previous sections. The time step size of the third-order accurate linearly-implicit Rosenbrock-type time integration scheme was 16 and 8 times larger than those used in [44] and [45], respectively. The relative defect tolerance for the linear solver reads $rTol = 10^{-5}$.

Once again we consider GMRES(MB)[BJ] as the reference solution strategy. Being the number of curved elements small when compared to the number of affine elements, the degrees of exactness of quadrature rules disregards the second degree geometrical representation of cells

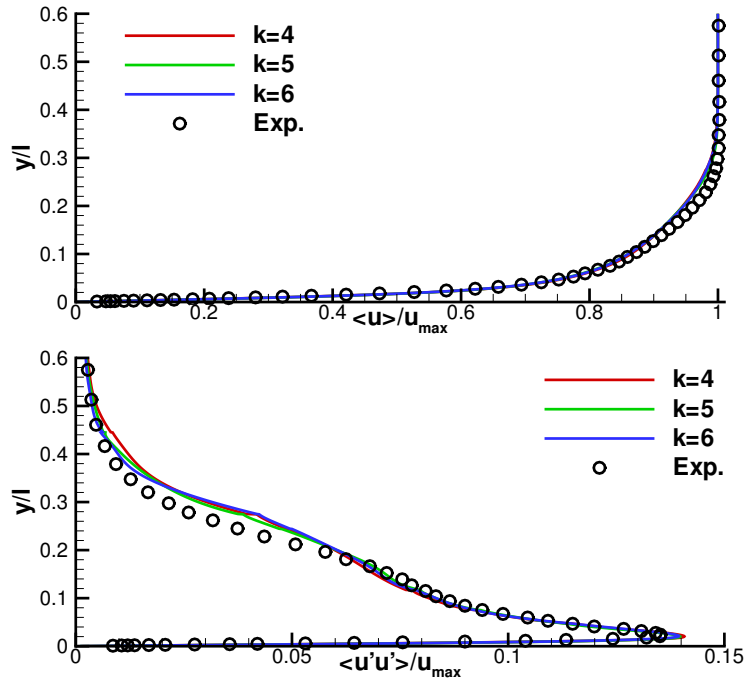


Figure 10: T3L1 test case, $k = 6$ solution for $Tu = 0.2\%$. Time- and spanwise-averaged velocity profiles in comparison with experimental data [51] at $x/l = 3.45$. Mean (top) and RMS (bottom) velocity.

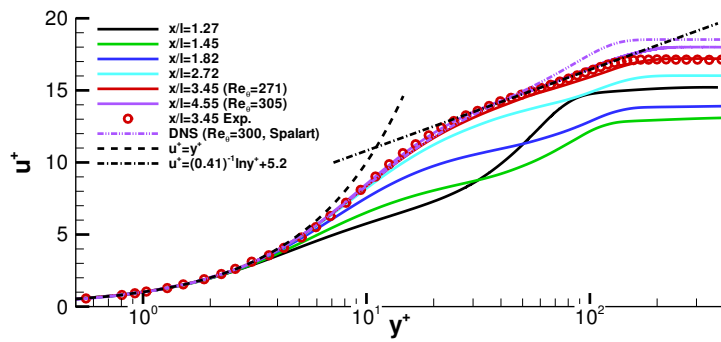


Figure 11: T3L1 test case, $k = 6$ solution for $Tu = 0.2\%$. Non dimensional stream-wise velocity profile for different values of x/l after reattachment in comparison to the theoretical law of the wall and DNS data [50].

close to leading edge. Since the boundary layer is still laminar at the leading edge, this under-integration does not affect stability of the scheme.

Switching from the matrix-based (GMRES(MB)[BJ]) to the matrix-free solver (GMRES(MF)[BJ]) we observe the same computational efficiency but 40% less memory usage. Note that the use of Additive Schwarz preconditioned GMRES (GMRES[ASM(1,ILU(0))]) decreases the overall parallel efficiency of the method. In fact, the CPU time increases by the 11% and the memory requirements raises by 60%.

The p -multigrid preconditioned solver specs are as follows: FGMRES(MB or MF) as outer solver, a full p -multigrid iteration with $L = 3$, $\kappa_\ell = 6, 2, 1$, GMRES(MB or MF)[EWBJ] smoother for $\ell = 0$ (8 iterations), GMRES(MB)[EWBJ] smoother for $\ell = 1$ (8 iterations) and GMRES(MB)[ASM(1,ILU(0))] smoother on the coarsest level ($\ell = 2$, 40 iterations). Note that for the finest level outer solver and smoother we consider both matrix-based and matrix-free implementations for the sake of comparison. The computational efficiency of the method improves considerably with respect to the reference (first column of Tab. 9): i) in a matrix-based framework a 50% decrease of the CPU time is observed and the memory requirements reduce by 35%, ii) in a matrix-free framework the CPU times gains are unaltered and the memory savings reach 85%. Such significant memory footprint reductions are mainly due the finest level strategy: only a block diagonal matrix is allocated and a small number of Krylov subspaces is employed for the GMRES algorithm. We remark that in this case the actual memory footprint has been computed through the PETSc library, and it is in line with the values that can be estimated a-priori using the model of Section 2.5.

As a further optimization of the matrix-free approach we consider the possibility to lag the computation of the system matrix employed for preconditioning purposes, this means that the preconditioner is “frozen” for several time steps. Clearly this strategy reduces assembly times but degrades convergence rates if the discrepancy between the matrix and the preconditioner gets too severe. In the present computation optimal performance are achieved by lagging the operators evaluation for 3 time steps. By doing so, the CPU time is further reduced to the 0.31 of the baseline, see Tab. 9, which corresponds to a speed-up of 3.22. As a side effect, the average number of GMRES iterations slightly increases, from 3.0 to 3.31, due to a loss of efficiency of the multigrid preconditioner.

| Solver Prec | GMRES(MB) BJ | GMRES(MB) ASM(1,ILU(0)) | GMRES(MF) BJ | FGMRES(MB) MG _{full} | FGMRES(MF) MG _{full} | FGMRES(MF) MG _{full} (LAG=3) |
|----------------|-----------------|----------------------------|-----------------|----------------------------------|----------------------------------|--|
| CPU Ratio | 1 | 1.11 | 0.95 | 0.50 | 0.47 | 0.31 |
| Memory Ratio | 1 | 1.6 | 0.6 | 0.65 | 0.15 | 0.15 |
| ITs | 115 | 72 | 115 | 3.0 | 3.0 | 3.31 |

Table 9: Performance comparison of the solver on the T3L1 test case. Computational time, total memory footprint non-dimensionalized with the GMRES(MB)[BJ] solver, and average number of GMRES iterations per time step, for the BJ, ASM(1,ILU(0)) and p -multigrid preconditioners (see text for settings details). Results obtained on 540 Intel Xeon CPUs of Marconi-A1@CINECA.

4. Conclusion

The paper presents a p -multigrid preconditioner strategy applied to the solution of linear system arising from linearly-implicit Rosenbrock-type time discretizations. The algorithm relies on a matrix-free implementation of both the outer FGMRES solver as well as the finest level smoother, while matrix-based GMRES smoothers are employed on coarse levels. Coarse operators of lower polynomial degree are built using a rescaled-inherited approach which provides optimal scaling of the stabilization terms and improves p -multigrid preconditioner's efficiency and robustness.

The performance of the algorithm has been evaluated on test cases of growing complexity. First, we tackle Poisson problems demonstrating the benefits of the rescaled-inherited approach introduced in [20] in a p -multigrid preconditioner strategy. Second, we deal with unsteady laminar flows, *i.e.*, the flow around a two-dimensional cylinder and a sphere, showing that the p -multigrid preconditioned solver outperform standard single-grid preconditioned iterative solvers from a CPU time viewpoint. We consider serial and parallel computations (up to 576 cores and 6 elements per partition), with speed-ups ranging from approximatively 1.5 to 3.5.

Finally, we perform ILES of the incompressible turbulent flow over a rounded-leading edge plate with different free-stream turbulent intensities. High-order accurate $k = 6$ solutions are compared with published numerical results and wind tunnel experiments. The solver strategy is profiled and compared with state-of-the-art single-grid solvers running on large HPC facilities. We show that, if a block-diagonal preconditioner is employed on the finest level, the algorithm reduces the memory footprint of the solver of about 92% of the standard matrix-based implementation. Interestingly, besides the remarkable memory savings, the p -multigrid preconditioned FGMRES solver is also three times faster than the best performing single-grid solver.

We remark that increasing the complexity of the problems has not required tuning of p -multigrid parameters confirming the robustness of the proposed approach. Future works involve the implementation of an adaptive strategy for the choice of the quadrature degree of exactness, which can be adapted in view of the actual amount of curvature of mesh faces, in order to optimise the computation of the residuals vector and thus the overall performance of the matrix-free algorithm.

Acknowledgements

We acknowledge the CINECA award, under the ISCRA initiative (grant numbers HP10BEE6C4, HP10CPSWZ2, HP10BMA1AP, HP10CKYRYE, HP10CE90VW), for the availability of high performance computing resources and support. Professor Michele Napolitano (Politecnico di Bari) and the co-authors of [51] are also gratefully acknowledged for sharing the experimental data of the T3L1 test case.

References

- [1] F. Bassi, L. Botti, A. Colombo, A. Crivellini, A. Ghidoni, F. Massa, On the development of an implicit high-order discontinuous Galerkin method for dns and implicit les of turbulent flows, *European Journal of Mechanics-B/Fluids* 55 (2016) 367–379.
- [2] J.-B. Chapelier, M. De La Llave Plata, F. Renac, E. Lamballais, Evaluation of a high-order discontinuous Galerkin method for the dns of turbulent flows, *Computers & Fluids* 95 (2014) 210–226.
- [3] C. C. Wiart, K. Hillewaert, L. Bricteux, G. Winckelmans, Implicit les of free and wall-bounded turbulent flows based on the discontinuous Galerkin/symmetric interior penalty method, *International Journal for Numerical Methods in Fluids* 78 (6) (2015) 335–354.

- [4] F. Bassi, A. Crivellini, D. Di Pietro, S. Rebay, An implicit high-order discontinuous Galerkin method for steady and unsteady incompressible flows, *Computers & Fluids* 36 (10) (2007) 1529–1546.
- [5] A. Uranga, P.-O. Persson, M. Drela, J. Peraire, Implicit large eddy simulation of transition to turbulence at low Reynolds numbers using a discontinuous Galerkin method, *International Journal for Numerical Methods in Engineering* 87 (1-5) (2011) 232–261.
- [6] F. Bassi, L. Botti, A. Colombo, A. Ghidoni, F. Massa, Linearly implicit Rosenbrock-type Runge–Kutta schemes applied to the discontinuous Galerkin solution of compressible and incompressible unsteady flows, *Computers & Fluids* 118 (2015) 305–320.
- [7] A. Crivellini, F. Bassi, An implicit matrix-free discontinuous Galerkin solver for viscous and turbulent aerodynamic simulations, *Computers & Fluids* 50 (1) (2011) 81–93.
- [8] A. Sarshar, P. Tranquilli, B. Pickering, A. McCall, C. J. Roy, A. Sandu, A numerical investigation of matrix-free implicit time-stepping methods for large CFD simulations, *Computers & Fluids* 159 (2017) 53–63.
- [9] M. Ceze, L. Diosady, S. M. Murman, Development of a high-order space-time matrix-free adjoint solver, in: 54th AIAA Aerospace Sciences Meeting, 2016, p. 0833.
- [10] M. Franciolini, A. Crivellini, A. Nigro, On the efficiency of a matrix-free linearly implicit time integration strategy for high-order discontinuous Galerkin solutions of incompressible turbulent flows, *Computers & Fluids* 159 (2017) 276–294. doi:<https://doi.org/10.1016/j.compfluid.2017.10.008>. URL <http://www.sciencedirect.com/science/article/pii/S0045793017303651>
- [11] A. Crivellini, M. Franciolini, A. Nigro, A matrix-free incompressible DG algorithm for the simulation of turbulent flows, in: *Progress in Turbulence VII*, Springer, 2017, pp. 153–159.
- [12] B. Helenbrook, D. Mavriplis, H. Atkins, Analysis of “p”-multigrid for continuous and discontinuous finite element discretizations, in: 16th AIAA Computational Fluid Dynamics Conference, 2003, p. 3989.
- [13] F. Bassi, S. Rebay, Numerical solution of the Euler equations with a multiorder discontinuous finite element method, in: *Computational Fluid Dynamics 2002*, Springer, 2003, pp. 199–204.
- [14] K. J. Fidkowski, T. A. Oliver, J. Lu, D. L. Darmofal, p-multigrid solution of high-order discontinuous Galerkin discretizations of the compressible Navier–Stokes equations, *Journal of Computational Physics* 207 (1) (2005) 92–113.
- [15] F. Prill, M. Lukáčová-Medvid'ová, R. Hartmann, Smoothed aggregation multigrid for the discontinuous Galerkin method, *SIAM Journal on Scientific Computing* 31 (5) (2009) 3503–3528.
- [16] M. Wallraff, R. Hartmann, T. Leicht, Multigrid solver algorithms for DG methods and applications to aerodynamic flows, in: *IDIHOM: Industrialization of High-Order Methods-A Top-Down Approach*, Springer, 2015, pp. 153–178.
- [17] P. F. Antonietti, M. Sarti, M. Verani, Multigrid algorithms for hp-discontinuous Galerkin discretizations of elliptic problems, *SIAM Journal on Numerical Analysis* 53 (1) (2015) 598–618.
- [18] K. Shahbazi, D. J. Mavriplis, N. K. Burgess, Multigrid algorithms for high-order discontinuous Galerkin discretizations of the compressible Navier–Stokes equations, *Journal of Computational Physics* 228 (21) (2009) 7917–7940.
- [19] L. T. Diosady, D. L. Darmofal, Preconditioning methods for discontinuous Galerkin solutions of the Navier–Stokes equations, *Journal of Computational Physics* 228 (11) (2009) 3917–3935.
- [20] L. Botti, A. Colombo, F. Bassi, h-multigrid agglomeration based solution strategies for discontinuous Galerkin discretizations of incompressible flow problems, *Journal of Computational Physics* 347 (2017) 382–415.
- [21] F. Bassi, S. Rebay, A high-order accurate discontinuous finite element method for the numerical solution of the compressible Navier–Stokes equations, *J. Comput. Phys.* 131 (1997) 267–279.
- [22] F. Brezzi, G. Manzini, D. Marini, P. Pietra, A. Russo, Discontinuous Galerkin approximations for elliptic problems, *Numer. Methods Partial Differential Equations* 16 (2000) 365–378.
- [23] D. N. Arnold, F. Brezzi, B. Cockburn, L. D. Marini, Unified analysis of discontinuous Galerkin methods for elliptic problems, *SIAM J. Numer. Anal.* 39 (5) (2002) 1749–1779.
- [24] F. Bassi, A. Crivellini, D. Di Pietro, S. Rebay, An artificial compressibility flux for the discontinuous Galerkin solution of the incompressible Navier–Stokes equations, *Journal of Computational Physics* 218 (2) (2006) 794–815. doi:[10.1016/j.jcp.2006.03.006](https://doi.org/10.1016/j.jcp.2006.03.006).
- [25] J. Lang, J. Verwer, ROS3P—An accurate third-order Rosenbrock solver designed for parabolic problems, *BIT* 41 (4) (2001) 731–738.
- [26] P. F. Antonietti, B. A. de Dios, S. C. Brenner, L. yeng Sung, Schwarz methods for a preconditioned WOPSIP method for elliptic problems, *Computational Methods in Applied Mathematics* 12 (3) (2012) 241–272. doi:[10.2478/cmam-2012-0021](https://doi.org/10.2478/cmam-2012-0021).
- [27] F. Brezzi, G. Manzini, D. Marini, P. Pietra, A. Russo, Discontinuous Galerkin approximations for elliptic problems, *Numer. Methods Partial Differential Equations* 16 (2000) 365–378.
- [28] D. Schötzau, C. Schwab, A. Toselli, Mixed hp-DGFEM for incompressible flows, *SIAM Journal on Numerical Analysis* 40 (6) (2002) 2171–2194. doi:[10.1137/S0036142901399124](https://doi.org/10.1137/S0036142901399124).
- [29] D. A. Di Pietro, A. Ern, *Mathematical Aspects of Discontinuous Galerkin Methods*, Vol. 69 of *Maths & Applica-*

- tions, Springer-Verlag, 2011.
- [30] T. Warburton, J. Hesthaven, On the constants in hp-finite element trace inverse inequalities, *Computer Methods in Applied Mechanics and Engineering* 192 (25) (2003) 2765 – 2773. doi:[https://doi.org/10.1016/S0045-7825\(03\)00294-9](https://doi.org/10.1016/S0045-7825(03)00294-9).
URL <http://www.sciencedirect.com/science/article/pii/S0045782503002949>
- [31] C. Schwab, *p- and hp- Finite Element Methods: Theory and Applications in Solid and Fluid Mechanics*, Numerical Mathematics and Scientific Computation, Clarendon Press, 1998.
- [32] Y. Saad, M. H. Schultz, GMRES: A generalized minimal residual algorithm for solving nonsymmetric linear systems, *SIAM J. Sci. Stat. Comput.* 7 (1986) 856–869.
- [33] D. Knoll, D. Keyes, Jacobian-free Newton-Krylov methods: a survey of approaches and applications, *J. Comput. Phys.* 193 (2) (2004) 357–397.
- [34] M. Pernice, H. Walker, Nitsol: A newton iterative solver for nonlinear systems, *SIAM Journal on Scientific Computing* 19 (1) (1998) 302–318.
- [35] A. Crivellini, F. Bassi, An implicit matrix-free discontinuous Galerkin solver for viscous and turbulent aerodynamics simulations, *Comput. & Fluids* 50 (1) (2011) 81 – 93.
- [36] S. Balay, J. Brown, K. Buschelman, W. D. Gropp, D. Kaushik, M. G. Knepley, L. C. McInnes, B. F. Smith, H. Zhang, PETSc Web page, <http://www.mcs.anl.gov/petsc> (2013).
- [37] J. Meneghini, F. Saltara, C. Siqueira, J. Ferrari Jr, Numerical simulation of flow interference between two circular cylinders in tandem and side-by-side arrangements, *Journal of fluids and structures* 15 (2) (2001) 327–350.
- [38] L. Botti, Influence of reference-to-physical frame mappings on approximation properties of discontinuous piecewise polynomial spaces, *Journal of Scientific Computing* 52 (3) (2012) 675–703.
- [39] T. Johnson, V. Patel, Flow past a sphere up to a Reynolds number of 300, *Journal of Fluid Mechanics* 378 (1999) 19–70.
- [40] A. G. Tomboulides, S. A. Orszag, Numerical investigation of transitional and weak turbulent flow past a sphere, *Journal of Fluid Mechanics* 416 (2000) 45–73.
- [41] P. Ploumhans, G. Winckelmans, J. K. Salmon, A. Leonard, M. Warren, Vortex methods for direct numerical simulation of three-dimensional bluff body flows: application to the sphere at $re = 300, 500, \text{ and } 1000$, *Journal of Computational Physics* 178 (2) (2002) 427–463.
- [42] A. Crivellini, V. D’Alessandro, F. Bassi, Assessment of a high-order discontinuous Galerkin method for incompressible three-dimensional navier-stokes equations: Benchmark results for the flow past a sphere up to $re = 500$, *Computers & Fluids* 86 (0) (2013) 442 – 458. doi:<http://dx.doi.org/10.1016/j.compfluid.2013.07.027>.
URL <http://www.sciencedirect.com/science/article/pii/S004579301300306X>
- [43] A. Crivellini, M. Franciolini, A. Colombo, F. Bassi, OpenMP parallelization strategies for a discontinuous Galerkin solver, *International Journal of Parallel Programming* 178 (2) (2018) 427–463.
- [44] M. Langari, Z. Yang, Numerical study of the primary instability in a separated boundary layer transition under elevated free-stream turbulence, *Physics of Fluids* 25 (7) (2013) 074106. doi:10.1063/1.4816291.
- [45] Z. Yang, P. R. Voke, Large-eddy simulation of boundary-layer separation and transition at a change of surface curvature, *Journal of Fluid Mechanics* 439 (2001) 305?333. doi:10.1017/S0022112001004633.
- [46] R. Hillier, N. Cherry, The effects of stream turbulence on separation bubbles, *Journal of Wind Engineering and Industrial Aerodynamics* 8 (1) (1981) 49 – 58. doi:[https://doi.org/10.1016/0167-6105\(81\)90007-6](https://doi.org/10.1016/0167-6105(81)90007-6).
- [47] Y. Nakamura, S. Ozono, The effects of turbulence on a separated and reattaching flow, *Journal of Fluid Mechanics* 178 (1987) 477?490. doi:10.1017/S0022112087001320.
- [48] Z. Yang, I. E. Abdalla, Effects of free-stream turbulence on a transitional separated?reattached flow over a flat plate with a sharp leading edge, *International Journal of Heat and Fluid Flow* 30 (5) (2009) 1026 – 1035, the 3rd International Conference on Heat Transfer and Fluid Flow in Microscale. doi:<https://doi.org/10.1016/j.ijheatfluidflow.2009.04.010>.
- [49] E. Lamballais, J. Silvestrini, S. Laizet, Direct numerical simulation of flow separation behind a rounded leading edge: Study of curvature effects, *International Journal of Heat and Fluid Flow* 31 (3) (2010) 295–306.
- [50] P. R. Spalart, Direct simulation of a turbulent boundary layer up to $re_\theta = 1410$, *Journal of Fluid Mechanics* 187 (1988) 61–98. doi:10.1017/S0022112088000345.
- [51] L. Cutrone, P. De Palma, G. Pascasio, M. Napolitano, Predicting transition in two-and three-dimensional separated flows, *International Journal of Heat and Fluid Flow* 29 (2) (2008) 504–526.